BBA - Bioenergetics 1860 (2019) 148084

Contents lists available at ScienceDirect

BBA - Bioenergetics

journal homepage: www.elsevier.com/locate/bbabio

# An alternative plant-like cyanobacterial ferredoxin with unprecedented structural and functional properties

Taiki Motomura[a,1], Lidia Zuccarello[b,c,1], Pierre Sétif[d], Alain Boussac[d], Yasufumi Umena[a], David Lemaire[b], Jatindra N. Tripathy[a,e], Miwa Sugiura[f], Rainer Hienerwadel[c,*], Jian-Ren Shen[a,*], Catherine Berthomieu[b,*]

[a] Research Institute for Interdisciplinary Science, Graduate School of Natural Science and Technology, Okayama University, Okayama 700-8530, Japan
[b] CEA, CNRS, Aix Marseille Univ, BIAM, Interactions Protéine Métal UMR 7265, 13108 Saint Paul-Lez-Durance, France
[c] Aix Marseille Univ, CEA, CNRS, BIAM, Luminy Genetics and Biophysic of Plants, UMR 7265, 13288 Marseille Cedex, France
[d] I2BC, UMR CNRS 9198, CEA Saclay, 91191 Gif-sur -Yvette, France
[e] Center for Biotechnology and Genomics, Texas Tech University, United States of America
[f] Proteo-Science Research Center, Ehime University, Bunkyo-cho, Matsuyama, Ehime 790-8577, Japan

ARTICLE INFO

*Keywords:*
Alternative ferredoxin
X-ray structure
UV–vis kinetics
Far-infrared of iron-sulfur center
Spectro-electrochemistry
Photosynthetic electron transfer

ABSTRACT

Photosynthetic [2Fe-2S] plant-type ferredoxins have a central role in electron transfer between the photosynthetic chain and various metabolic pathways. Several genes are coding for [2Fe−2S] ferredoxins in cyanobacteria, with four in the thermophilic cyanobacterium *Thermosynechococcus elongatus*. The structure and functional properties of the major ferredoxin Fd1 are well known but data on the other ferredoxins are scarce. We report the structural and functional properties of a novel minor type ferredoxin, Fd2 of *T. elongatus*, homologous to Fed4 from *Synechocystis* sp. PCC 6803. Remarkably, the midpoint potential of Fd2, Em = −440 mV, is lower than that of Fd1, Em = −372 mV. However, while Fd2 can efficiently react with photosystem I or nitrite reductase, time-resolved spectroscopy shows that Fd2 has a very low capacity to reduce ferredoxin-$NADP^+$ oxidoreductase (FNR). These unique Fd2 properties are discussed in relation with its structure, solved at 1.38 Å resolution. The Fd2 structure significantly differs from other known ferredoxins structures in loop 2, N-terminal region, hydrogen bonding networks and surface charge distributions. UV–Vis, EPR, and Mid- and Far-IR data also show that the electronic properties of the [2Fe−2S] cluster of Fd2 and its interaction with the protein differ from those of Fd1 both in the oxidized and reduced states. The structural analysis allows to propose that valine in the motif $Cys_{53}ValAsnCys_{56}$ of Fd2 and the specific orientation of Phe72, explain the electron transfer properties of Fd2. Strikingly, the nature of these residues correlates with different phylogenetic groups of cyanobacterial Fds. With its low redox potential and its discrimination against FNR, Fd2 exhibits a unique capacity to direct efficiently photosynthetic electrons to metabolic pathways not dependent on FNR.

## 1. Introduction

Ferredoxins (Fd) are ubiquitous proteins with major roles in bioenergetics. In organisms performing oxygenic photosynthesis, the soluble electron acceptors that function as a relay in the electron transfer between Photosystem I (PSI) in the photosynthetic chain and a number of soluble enzymes are Fds containing a redox active [2Fe−2S] cluster coordinated by four cysteine residues [1]. They are notably involved in the photosynthetic production of NADPH *via* the ferredoxin-NADP+ oxidoreductase (FNR) [2], and in cyclic electron transfer around PSI for the generation of a proton gradient used for ATP synthesis [3]. They are also involved in redox reactions associated with a large number of metabolic pathways such as $CO_2$ fixation, nitrogen or sulfur assimilation by reduction of nitrite reductase (NiR) or sulfite reductase [4–6] or in fatty acid or amino acid synthesis and redox regulation *via* the Fd-thioredoxin oxidoreductase. These plant-type Fds have a remarkably low midpoint potential in the −300 to −460 mV range *vs* NHE[2] [7–9].

Multiple gene copies for [2Fe−2S] Fds are present in the known genomes of plants, cyanobacteria and algae. For example, there are five genes coding for five Fds, noted Fed1 to Fed5 in the *Synechocystis* sp.

* Corresponding authors.
*E-mail addresses:* rainer.hienerwadel@univ-amu.fr (R. Hienerwadel), shen@cc.okayama-u.ac.jp (J.-R. Shen), catherine.berthomieu@cea.fr (C. Berthomieu).
[1] Equally contributed.
[2] All values of redox potentials are given with respect to the normal hydrogen electrode (NHE).

https://doi.org/10.1016/j.bbabio.2019.148084
Received 8 July 2019; Received in revised form 2 September 2019; Accepted 8 September 2019
Available online 12 September 2019

**Table 1**
Sequence alignment of the [2Fe−2S] ferredoxins from *T. elongatus* (noted Fd1 to Fd4) with those of *Synechocystis* sp. PCC 6803 (noted Fed1 to Fed4) and that of the main ferredoxin FdN of *Nostoc* PCC7120. The cysteine residues involved in the coordination of the iron-sulfur cluster are indicated in red. The additional cysteine residues are indicated in green. Fds from *T. elongatus*, *Synechocystis* sp. PCC 6803 and FdN from *Nostoc* PCC7120 have been grouped according to their sequence homologies.

```
                                                                  39       48   53
FdN Nos  all4148          MATFKVTLINEAE       GTKHEIEVPDDEYILDAAEEQGYDLPFSCRAGACS
Fd1 T el tsl1009  ------MATYKVTLVRPD-G------SETTIDVPEDEYILDVAEEQGLDLPFSCRAGACS
Fed1 Syn ssl0020  ------MASYTVKLITPD--------GESSIECSDDTYILDAAEEAGLDLPYSCRAGACS

Fd2 T el tlr1236  MTKRDHNKVYNVTLVNEERG------LNKTIRVHADEYILDAAEAQGIPLPYSCRAGACV
Fed4 Syn slr0150  -----MGAIYSVNLVNPATG------SDVTIEVAEDELILEAAENQGLDLPYSCRAASCV

Fd3 T el tlr1656  ---MSTPQTYTVTIHVRPLKSEDPPPRTYTITVPSDRYILQHAESQGLELPFSCRNGACT
Fed2 Syn sll1382  -----MSRSHRVLIHDRQNE------KDYSVIVSDDRYILHQAEDQGFELPFSCRNGACT

Fd4 T el tll0487  -----MTQTFRVEILHQG--------QTYTFEASADKPLLRSATAAGIDLPSSCNAGVCT
Fed3 Syn slr1828  -----MVNTYTAEIQHQG--------QTYTISVPEDKTVLQAADDEGIQLPTSCGAGVCT
                           . . :               :.    *  :*  *   *: ** **   . *
                  56               72            86           (Fd2 numbering)
FdN Nos  all4148  TCAGKLVSGTVDQSD--QSFLDDDQIEAGYVLTCVAYPTSDVVIQTHKEEDLY
Fd1 T el tsl1009  TCAGKLLEGEVDQSD--QSFLDDDQIEKGFVLTCVAYPRSDCKILTNQEEELY-------
Fed1 Syn ssl0020  TCAGKITAGSVDQSD--QSFLDDDQIEAGYVLTCVAYPTSDCTIETHKEEDLY-------

Fd2 T el tlr1236  NCAGRIIKGTVDQSD--HSFLKPKELDAGFVLLCAAYPTSDCVISTHEEDNLLNLA----
Fed4 Syn slr0150  ACAGRLLEGTVEHTDKGSDFLKPEELAAGCVLLCAAYATSDCKILTHQEEALFG------

Fd3 T el tlr1656  TCAVRILSGHVYQPE--AMGLSPALQAQGYALLCVSYARSDLEVETQDEDEVYELQFGRY
Fed2 Syn sll1382  ACAVRVISGQIHQPE--AMGLSPDLQRQGYALLCVSYAQSDLEVETQDEDEVYELQFGRY

Fd4 T el tll0487  TCAAQIQEGTVDHGD--AMGLSPELREKGYVLLCVARPCSDLKLISEKEEEVYNFQFGQ-
Fed3 Syn slr1828  TCAALITEGTAEQAD--GMGVSAELQAEGYALLCVAYPRSDLKIITEKEDEVYQRQFG—
                   **         : :     :.      * .* *.: . **  : : .*: :

FdN Nos  all4148  ---------------
Fd1 T el tsl1009  ---------------
Fed1 Syn ssl0020  ---------------

Fd2 T el tlr1236  ---------------
Fed4 Syn slr0150  ---------------

Fd3 T el tlr1656  FGKGRVQLGLPLDED
Fed2 Syn sll1382  FGAGRVRLGLPLDED

Fd4 T el tll0487  FQKA-----------
Fed3 Syn slr1828  -GQG-----------
```

PCC 6803 genome [5] and four genes coding for four Fds, noted here Fd1 to Fd4, in the genome of *Thermosynechococcus elongatus* [10], according to their degree of homology with petF. The sequence of Fd1 (*T. elongatus* gene *tsl1009*) presents a high homology with Fed1 in *Syn.* 6803 [5] as well as with the main Fd of *Nostoc* PCC7120, denoted thereafter FdN (Table 1). These Fds are the major proteins involved in photosynthetic electron transfer. From the gene sequence, Fd2 (*T. elongatus* gene *tlr1236*) has a higher molecular mass and presents a higher sequence homology with Fed4 of *Syn.* 6803 (Table 1), although it is not mentioned in [5]. Fd3 (*T. elongatus* gene *tlr1656*) presents a high sequence homology with Fed2 of *Syn.* 6803 with a C-terminal extension, while Fd4 (*T. elongatus* gene *tll0487*) is more closely related to the Fed3 of *Syn.* 6803. All these Fds have the typical $CysX_4CysX_2CysX_{29}Cys$ motif of plant-type ferredoxins involved in the binding of the [2Fe−2S] cluster, except Fed4 with $X_{31}$. In Fd1 and Fd2 from *T. elongatus*, there is a fifth cysteine (Cys87 in Fd1) not involved in the coordination of the [2Fe−2S] cluster. This Cys is also present in Fed1 and Fed4 from *Syn.* 6803, but is absent in the other Fds listed in Table 1, in particular in FdN.

While the electron transfer properties of the Fd1-type ferredoxins are well known, pieces of information on the other Fds remain scarce. Open questions include whether some of these Fds are in part redundant or if they are involved in preferential interactions with different partners, or even if they are involved in non-photosynthetic processes. In *Arabidopsis thaliana*, two photosynthetic Fds with contrasted abundance, AtFd1 7% and AtFd2 90%, have very similar redox potentials (at ≈ − 430 mV) and electron transfer kinetics with redox partners, and their different functions were proposed to be related to different expression patterns [11]. In *C. reinhardtii* and *Syn.* 6803, different functions of the Fds have been associated to different environmental conditions, different interaction efficiencies and electron transfer kinetics with the various Fd-dependent enzymes [5,12]. Very recently, Fed2 from *Syn.* 6803 corresponding to Fd3 from *T. elongatus* has been shown to have a high redox potential (at −243 mV) and not to be involved in photosynthetic electron transport, but in the response to changing environmental iron concentrations [13]. Data on the structure-function relationships of other minor Fds are lacking for a better understanding of their physiological roles and of the molecular mechanisms that eventually govern the transfer of photosynthetic electrons to different metabolic pathways.

The structure-properties relationship in Fds has been extensively studied for FdN. Its structure was solved in the oxidized (PDB ID: 1FXA, 1QT9) and reduced states (PDB ID: 1CZP) [14,15] as well as in complex with the redox partners FNR (PDB ID: 1EWY) [16] and PSI (PDB ID: 2PVO) [17]. In addition, studies of site directed mutants pointed key residues of FdN, Glu94 and Phe65, for efficient electron transfer to FNR [18]. The structure of *T. elongatus* Fd1, first studied by NMR [19,20], was recently solved by X-ray crystallography at 1.5 Å resolution (PDB ID: 5AUI) [21] and at 4.3 Å resolution in complex with PSI [17]. In contrast, no structures of minor Fds have been reported so far.

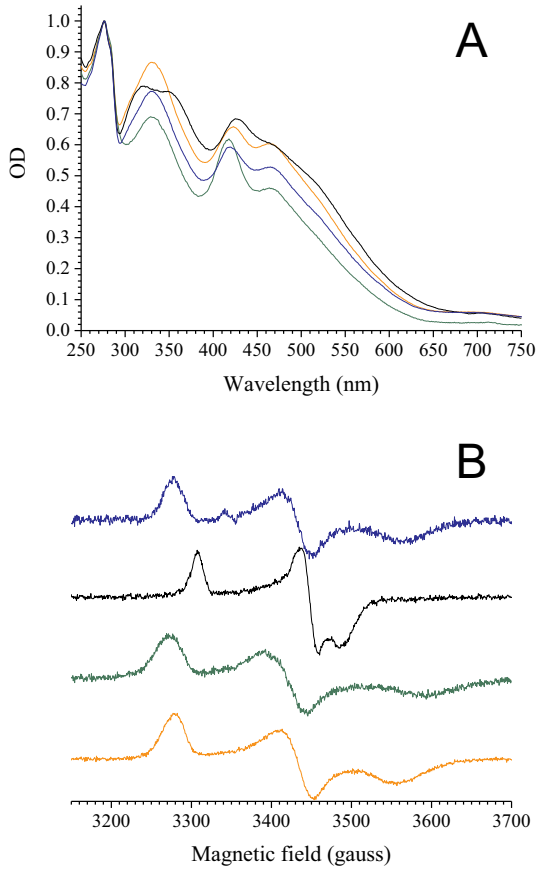


**Fig. 1.** UV–Vis absorption spectra (Panel A) and EPR spectra (Fds in the reduced form, Panel B) of Fd1 (orange), Fd2(green), Fd1' (black) and FdN (blue).

In this study, we studied the structural and functional properties of the minor-type Fd2 from *T. elongatus*. We purified Fd2, crystallized and solved its crystal structure at a 1.38 Å resolution. For comparison, we also determined the crystal structure of Fd1 from the same cyanobacterium at 1.55 Å resolution. We further examined the redox, electronic, and vibrational properties of Fd2 as well as its electron transfer (ET) properties with main potential partners PSI, FNR, and NiR, and compared them with those of Fd1, FdN, and of a minor Fd fraction likely resulting from Fd1 post-translational modification and noted thereafter Fd1'.

Our data show significant structural differences between Fd2 and Fd1, and indicate that Fd2 is the first example of a Fd with low redox midpoint potential that can efficiently react with PSI or NiR, but discriminates against FNR. The Val residue in the $Cys_{53}$ValThr$Cys_{56}$ motif of Fd2 and a completely different orientation of Phe72 in Fd2 as compared to that of the corresponding Phe65 in Fd1, are proposed to account for these unique properties of Fd2, and possibly of a group of phylogenetically related ferredoxins identified in cyanobacteria only.

## 2. Methods

### 2.1. Purification of the ferredoxins from Thermosynechococcus elongatus and Nostoc PCC7120

After harvesting, the cells were washed in a medium containing 10 mM Tricine and 15 mM $CaCl_2$, pH 7.5 and resuspended in ~100 mL of the same medium. Then the cells were broken by using a French press in the presence of DNaseA and anti-proteases (benzamidine and 6-aminocaproic acid). The broken cells were diluted into ~2 L of 18 MΩ water and ammonium sulfate was added to reach a final concentration of 45%. The mixture was gently stirred for 30 min at room temperature and then centrifuged for 30 min at room temperature (rotor Beckman Coulter JA10, 9500 RPM). The pellet containing the membranes and a large part of the phycobiliproteins was discarded. The supernatant was gently collected and passed through a Phenyl-Sepharose fast flow resin, equilibrated with 45% ammonium sulfate in water, at a flow rate of ≈6 mL/min. The proteins were then eluted with 1.6% ammonium sulfate in water at a flow rate of ≈0.5 mL/min. The remaining phycobiliproteins bound to the resin were then eluted with pure water and discarded. The proteins eluted from the Phenyl-Sepharose fast flow resin were concentrated by using an Amicon Ultra-15 Centrifugal Filter Unit (cut-off 3 kDa). The concentrated proteins were then loaded on a HiPrep Phenyl HP 16/10 column after the addition of 30% ammonium sulfate. A gradient from 30% to 0% ammonium sulfate in the presence of 10 mM tricine at pH 7.5, was applied in 45 min at a flow rate of 2 mL/min and several fractions were collected. A fraction containing some Fds (dark-brown fraction) eluted first, before a fraction containing mainly $Cytc_{550}$ (red fraction) and a fraction containing $Cytc_6$ (pink fraction).

The first dark-brown fraction was then loaded onto a HiTrap (Q-sepharose) ion-exchange column and the proteins were eluted with a NaCl gradient from 0 mM to 600 mM NaCl in the presence of 10 mM tricine pH 7.5 at a flow rate of 2 mL/min in 45 min. Two dark-brown fractions were found. One eluted between 200 mM and 300 mM NaCl and the other between 500 mM and 600 mM NaCl. Both contain Fd1 but the first fraction contains Fd1 and many other proteins (likely reflecting non-specific interactions).

The red fraction obtained from the Hi-trap column was concentrated to a volume of 2 ml. Then, it was loaded onto a gel filtration column (Sephadex 75, HiLoad 26/60Pharmacia). The proteins were eluted at a flow rate of 1 mL/min. The elution medium contained 10 mM tricine pH 7.5, 50 mM NaCl. The gel filtration gave several peaks (yellow, red, pink, dark-brown) which were collected separately. Each of these fractions was then separately loaded onto a HiTrap (Q-sepharose) column and the proteins were eluted with a NaCl gradient (in the presence of 10 mM tricine pH 7.5) from 0 mM to 600 mM at 2 ml/min in 45 min. Fd2 was eluted from several of the pools at approximately 250 mM NaCl. Other proteins were found in the following order: $Cytc_6$ox at 40 mM, $Cytc_6$red at 80 mM, PsbV2 at 200 mM, $Cytc_{550}$ at approximately 300 mM [22], Fd1 at 500–600 mM NaCl. Finally, all the fractions found above were separately concentrated and washed in 10 mM tricine pH 7.5. Each of the concentrated proteins was then separately loaded onto a MonoQ column for a final purification step. Elution of the proteins was done with a NaCl gradient from 0 to 600 mM in the presence of 10 mM tricine pH 7.5 at a flow rate of 0.5 ml/min during 45 min. The purity of the fractions was estimated from the absorption spectra (see Fig. 1A).

### 2.2. Preparation of other proteins

Photosystem I from *T. elongatus* was purified as previously described [23]. An N-truncated form of FNR from *T. elongatus*, lacking the first 85 residues, was overexpressed in *E. coli* and purified similarly to the short FNR isoform from *Syn.* 6803 [24]. Partial alignment with this short isoform is shown below (genes slr1643 and tlr1211 for *Syn.* 6803 and *T. elongatus*, respectively). The truncated FNR isoform thus begins with alanine 86, as confirmed by mass spectrometry (not shown).

slr1643 MTTTPKEKKADDIPVNIYRP...
tlr1211 ..AAPVKEKKVDIPVNIYRP...

This FNR protein is similar in size and sequence to the short FNR isoform $FNR_S$ from *Syn.* 6803. Contrary to the case of *Syn.* 6803 where two FNR isoforms of different sizes are expressed from a single gene [25], no short isoform is present *in vivo* in *T. elongatus*, in which only the large isoform $FNR_L$ bound to phycobilisomes is expressed [26]. $FNR_S$ and a phycobilisome subcomplex $FNR_L$-phycocyanin ($FNR_L$-PC), both from *Syn.* 6803, were previously compared regarding their functional properties [27]. Two differences that are relevant to the present study

were observed: the midpoint potential $E_m$ corresponding to the first FNR reduction is 6 mV higher in $FNR_L$-PC than in $FNR_S$; the rate constant $k_{on}$ of $Fd_{red}$ association to FNR is 40% smaller with $FNR_L$-PC than with $FNR_S$. Whereas the change in $E_m$ is negligible, the change in $k_{on}$, although significant, indicates that in the presence of PC, the interaction between Fd and FNR is not dramatically disturbed. In turn, this shows that comparing the reactivity of the pseudo-short FNR from *T. elongatus* with Fd1 and Fd2 is relevant.

Recombinant NiR from *Chlamydomonas reinhardtii* was overexpressed in *E. coli* and purified as previously described [28].

### 2.3. Crystallization and X-ray data collection

The protein concentration of Fd1 and Fd2 was measured by the BCA method with a BCA Protein Assay Kit (TaKaRa, Japan). The absorption peak at 562 nm was measured by a UV–visible spectrophotometer UV-2450 (Shimazu). The Fd1 sample at a concentration of 8 mg/ml was mixed at a ratio of 1 to 1 with a reservoir solution containing 100 mM sodium citrate (pH 6.5), 2.6 M ammonium sulfate, 0.2% benzamidine hydrochloride and 1,6-hexanediol according to the previous report [21], and crystallized by the vapor-diffusion method for several weeks at 20 °C. The Fd1 crystals obtained were cryo-protected using the same solution as that of the reservoir plus 10% (w/v) glycerol, and flash frozen with a cooled nitrogen gas. X-ray diffraction data for Fd1 were collected at Beamline BL41XU of SPring-8 at a wavelength of 1.000 Å at 100 K.

For crystallization of Fd2, the Fd2 sample at a concentration of 8 mg/mL was mixed at a ratio of 3 to 1 with a reservoir solution containing 100 mM HEPES (pH 7.5) and 2.4 M ammonium sulfate, and crystallized also by the vapor-diffusion method for several weeks at 20 °C. Aggregated needle-like crystals mixed with a thin plate crystal were obtained. The crystal has a brown color due to the iron from the ferredoxin. They were cryo-protected using the same solution as that of the reservoir plus 15% (w/v) glycerol, and flash frozen with a cooled nitrogen gas. X-ray diffraction data for Fd2 were collected at Beamline BL38XU of SPring-8 at a wavelength of 1.000 Å at 100 K. The X-ray doses of each collection were calculated by RADDOSE-3D [29] using a solvent content calculated by Cell Content Analysis of CCP4 [30].

### 2.4. Structure determination

Diffraction data were indexed, integrated, and scaled by XDS [31]. The structure factors were generated using the program truncate in CCP4 [32]. The initial phases were obtained by the molecular replacement method using Molrep [33] with the structure of the major Fd1 from *T. elongatus* (PDBID: 5AUI [21]) as the search model, which results in a model having 97 residues. The rest of the model was manually built with the program COOT [34], and the structure refinement was performed with the program Refmac [35]. Ramachandran plot was calculated with MolProbity [36]. The secondary structure of Fd2 was assigned by DSSP [37,38] on Pymol plugin [39]. The statistics of X-ray diffraction data and structural refinement were summarized in Supp. Table 1. The structure of Fd1 was determined to a resolution of 1.55 Å with the same method as that described for Fd2 (structure parameters are given in Supp. Table 1).

### 2.5. Sequence alignment and structure comparison

The amino acid sequences of the ferredoxin proteins from *T. elongatus* were searched using cyanobase of the Kazusa research institute [10] and aligned with ClustalW [40,41]. Superposition of the ferredoxin structures was performed with COOT [34,42] with the SSM Superpose function [43] for comparison between the whole structures of Fds. The surface charges of the ferredoxin structures were generated by APBS Electrostatic [44] of the Pymol plugin [39]. The secondary structure assignments of Fds were performed by DSSP [37,38] on the DALI Server [45]. For docking simulation, GRAMM-X was used [46,47]. RMSDs (Root-Mean Square Deviations) between Cα atoms of different Fds were calculated using lsqkab [48].

### 2.6. Mass spectrometry experiments

Fd2 was initially identified by MALDI-TOF/MS measurements in the linear mode as previously described [49]. Then, mass analysis of the Fds was done in more gentle conditions using a MicroTOF-Q (Bruker, Wissembourg, France) Mass Spectrometer equipped with an electrospray ionization source. In denaturing conditions, samples concentrations were 1 µM in $CH_3CN/H_2O$ (1/1-v/v), 0.2% formic acid (Sigma-Aldrich). Samples were continuously infused at a flow rate of 3 µL $min^{-1}$. Mass spectra were recorded in the 50–7000 mass-to-charge (*m/z*) range. MS experiments were carried out with a capillary voltage set at 4.5 kV and an end plate off set voltage at 500 V. The gas nebulizer ($N_2$) pressure was set at 0.4 bar and the dry gas flow ($N_2$) at 4 L $min^{-1}$ at a temperature of 190 °C.

Non-covalent mass spectrometry measurements were performed to identify and determine stoichiometry of complexes. The samples at a concentration of 5 or 10 µM in 20 mM ammonium acetate (Sigma-Aldrich) were continuously infused at a flow rate of 7 µL $min^{-1}$. The mass spectra were recorded in the 50–4000 mass-to-charge (*m/z*) range. The gas nebulizer ($N_2$) pressure was set at 3 bars and the dry gas flow ($N_2$) at 3 L $min^{-1}$ at a temperature of 200 °C.

Data were acquired in the positive mode and calibration was performed using a calibrating solution of ESI Tune Mix (Agilent) in $CH_3CN/H_2O$ (95/5-v/v). The system was controlled with the software package MicrOTOF Control 2.2 and data were processed with DataAnalysis 3.4.

### 2.7. Sample preparation for electrochemistry and FTIR spectroscopy

All protein samples (Fd1, Fd2 and Fd1' from *T. elongatus* and FdN from *Nostoc PCC7120*) were concentrated to 0.2 to 3 mM in tricine 50 mM, NaCl 100 mM, pH 7.5 or CAPS 50 mM, NaCl 100 mM, pH 10. To prepare the $^2H_2O$ samples, the $H_2O$ buffers were lyophilized and returned to the original volume using $^2H_2O$, twice in a row. Two concentration / dilution steps using the $^2H_2O$ buffers on Amicon 3 kDa membranes were employed to prepare the samples.

### 2.8. Spectro-electrochemistry

Spectro-electrochemistry was performed using the three-electrode thin path-length cell described in [50] equipped with $CaF_2$ or CVD diamond windows. This cell is air-tight and allows recording spectra in the whole UV-to far-IR spectral region. The working electrode is a 4 µm-thick gold grid washed with a ($H_2SO_4$:$H_2O_2$ 3:1) solution, then surface-modified by dipping it for 20 min into a 5 mM pyridine-3-carboxaldehyde thiosemicarbazone solution heated to 80–90 °C. The path-length of the cell was adjusted below 10 µm using the sample absorption at 1640 $cm^{-1}$. The following list of mediators was used to accelerate the redox reactions: methyl viologen (MV, $E^0$: −444 mV/NHE), benzyl viologen ($E^0$: −358 mV), anthraquinone 2-sulfonate ($E^0$: −223 mV), 2-hydroxy 1,4-naphtoquinone ($E^0$: −123 mV), 2,5-dihydroxy p-benzoquinone ($E^0$: −60 mV), duroquinone ($E^0$: +10 mV), N-ethyldibenzopyrazine(ethyl)sulfonate ($E^0$: +55 mV), methylphenazinium methyl salt ($E^0$: +80 mV), 1,2-naphtoquinone 4-sulfonic acid ($E^0$: +217 mV), diaminodurol ($E^0$: +240 mV), tetramethylphenylene-diamine ($E^0$: +270 mV), 2,5-dichloro 1,4-benzoquinone ($E^0$: +300 mV) and ferricyanide ($E^0$: +426 mV). The final concentration of each mediator was 40 µM. Equilibrium redox titrations were performed by applying potentials ranging from −190 mV to −490 mV *vs* NHE for Fd1 and the ferredoxin from *Nostoc* PCC7120, from −270 mV to −570 mV for Fd2, and from −170 mV to −530 mV for Fd1', with 20 mV intervals. Externally triggered potentiostats EG&G 262 or

Tacussel Polarostat Type PGRE were used for the redox titrations. Each potential was applied for 10 min before recording the UV–Vis spectra.

### 2.9. UV–Vis and EPR spectroscopy

Absorption spectra during the purification of the Fds were measured with an Uvikon XL Secomam (Bioserv) spectrometer. For the redox titrations, the UV–Vis spectra were recorded in the 390 to 660 nm range, using a Cary 14 spectrophotometer. The electrochemical cell was thermostated at 15 °C with a water circulation system and the sample compartment was purged with dry air to avoid water vapor condensation. The data were analysed using the integrated spectral area from 390 to 640 nm.

X-band cw-EPR spectra were recorded with a Bruker Elexsys 500 X-band spectrometer equipped with a standard ER 4102 (Bruker) X-band resonator, a Bruker teslameter, an Oxford Instruments cryostat (ESR 900) and an Oxford ITC504 temperature controller.

### 2.10. FT-IR difference spectroscopy

Mid-IR FTIR difference spectra were recorded using a Bruker Tensor 27 spectrophotometer equipped with a MCT detector and purged with dry air. Spectra from 680 to 100 $cm^{-1}$ were recorded using a vacuum-purged Bruker Vertex 70v spectrophotometer equipped with a helium-cooled Si-Bolometer. Electrochemistry was performed at 10 °C and spectra were recorded after 10 or 15 min equilibration at the oxidizing (−190 mV) or reducing (−650 mV) potentials. For each electrochemical cycle, reduced-*minus*-oxidized or oxidized-*minus*-reduced spectra corresponded to the average of 300 scans. The final reduced-*minus*-oxidized difference spectra correspond to the average of spectra obtained with 10 to 20 electrochemical cycles in the Mid-IR and 20 to 30 electrochemical cycles in the Far-IR.

### 2.11. Flash-absorption spectroscopy

Measurements were made at 22 °C in 1-cm square cuvettes with a DC-0.3 MHz bandwidth. Actinic laser excitation (7 ns duration at 700 nm, 15 mJ energy), which is saturating for PSI photochemistry, was provided by a dye laser (Sirah-Lasertechnik) pumped by a frequency-doubled:YAG laser (Spectra-Physics). Experiments were performed at a few wavelengths, which were selected by 10-nm bandwidth interference filters placed before and after the cuvette. Measurements at 800 nm (data not shown) were made to quantify the PSI concentration, using an absorption coefficient of 7700 $mM^{-1}$ $cm^{-1}$ for $P700^+$ [24]. Fd reduction by PSI was measured at 580 nm. Indeed, at this wavelength often used in previous studies [51,52], PSI absorbs very weakly and 580 nm is close to the isosbestic point of β-carotene triplet states ($^3$car), which decay in the same time range as the fast phases of Fd reduction. The same wavelength was used for studying reduction of FNR by reduced Fd ($Fd_{red}$) as FADH·, the protonated radical of singly-reduced FNR, absorbs strongly at this wavelength [53]. NiR reduction by $Fd_{red}$ was studied at 520 nm, where this process gives a large absorption change [54], contrary to 580 nm. In the visible region (520 and 580 nm), actinic effects of the measuring light were avoided by a shutter, which was placed just before the cuvette and opened 1 ms before the actinic laser flash. All measurements were performed in 20 mM Tricine, 0.03% β-dodecyl-maltoside, 2 mM sodium ascorbate and 25–30 μM 2,6-dichlorophenolindophenol (DCPIP). DCPIPH2 (DCPIP reduced by ascorbate) completely reduces $P700^+$ in a few seconds, which allowed signal averaging at a frequency of 0.1 to 0.14 Hz. Fd and FNR measurements were performed in the presence of 5 mM $MgCl_2$ and 30 mM NaCl. NiR measurements were performed in the presence of 0.5 M mannitol, 2 mM $MgCl_2$ and 15 mM NaCl.

In experiments at 520 and 580 nm, a reference and a sample cuvette were placed alternatively in the cuvette holder. For studying Fd reduction by PSI, the reference cuvette contains only PSI so that the recording of the signal from the reference cuvette signal allows the large absorption changes due to $P700^+$ formation to be subtracted, as well as the absorption changes due to reduction of the terminal PSI acceptor ($F_A$ and $F_B$). Moreover, the absorption changes due to the triplet carotenoid decay are also eliminated. For studying FNR or NiR reduction by Fd, the reference cuvette contains PSI and Fd. By subtracting the reference cuvette signal, one can additionally eliminate the kinetics of Fd reduction by PSI. The signals shown in the main text and in Supporting Information are the averages of 24 to 32 measurements.

### 2.12. Phylogenetic analysis

The sequences of [2Fe-2S] Fds from most cyanobacteria were obtained with the BLAST tool from JGI-IMG [55] by searching in 83 cyanobacterial "finished" genomes using the Fd1 sequence. Sequences from [2Fe−2S] Fds from maize, *Arabidopsis thaliana* and *Chlamydomonas reinhardtii* were retrieved from Uniprot [56]. Sequence alignments were made with MUSCLE and phylogenetic tree constructions with the neighbor-joining method, both provided in the SeaView integrated software V 4.7 [57]. In both cases, default parameters were used. Phylogenetic trees were visualized with ITOL [58].

## 3. Results

### 3.1. Mass spectrometry

Fd1 and Fd2 were identified by their molecular masses determined at 10,714.45 Da and 11,729.5 Da by ESI-MS (Table 2, Supp. Fig. 1). In whole cells, the ratio between Fd2 and Fd1 was estimated at 5% considering similar extinction coefficients for Fd1 at 425 nm and Fd2 at 418 nm [59] and neglecting possible loss of proteins during purification. Fd2 is thus a minor Fd in *T. elongatus*. During purification, we found a very small fraction containing a Fd with specific electronic and EPR properties. The experimental mass of this protein determined by ESI-MS in the native mode corresponded to Fd1 with the [2Fe−2S] cluster and a + 32 Da mass adduct (Supp. Fig. 1). This protein fraction likely corresponds to a post-translationally modified Fd1 and it was denoted Fd1'. The mass adduct was less present in the denaturing mode (Supp. Fig. 1) and lost upon reduction of Fd1' by dithionite (data not shown). It could correspond to a peroxidation or a persulfidation with the formation of a CysSSH side chain [60], since both modifications are prone to reversion [61]. Fd1' could be the result of oxidative stress or a Fd fraction involved in signalization, since cysteine persulfidation was identified as a possible relay in $H_2S$ signaling ([60] and refs therein). The results obtained with Fd1' are provided to the reader despite the fact that the small amount of Fd1' did not enable some experiments to be performed for its characterization.

### 3.2. UV–visible spectra

The UV–Vis absorption spectra of the oxidized forms of Fd1, Fd1', Fd2 and FdN are all typical of [2Fe-2S] type Fds and indicate a high degree of purity for the proteins (Fig. 1A) [59]. Fd1 and FdN have almost identical UV–Vis spectra, with three main absorptions at 330, 425, and 470 nm and a shoulder at ≈520 nm. Fd2 shows a hypsochromic shift and a larger relative amplitude for the band at 418 nm, *versus* 425 nm for Fd1 and FdN. The spectrum of Fd1' differs by a split of the UV band in two contributions at 320 and 355 nm, a slight bathochromic shift of the band at 428 nm and a larger relative amplitude of the 520–530 nm shoulder. The small changes in the near-UV and visible parts of the spectra are indicative of different electronic structures of the [2Fe−2S] clusters and hence of different interactions between the cluster and the protein.

**Table 2**
Main properties of the ferredoxins of *T. elongatus* Fd1, Fd2 and Fd1' compared to FdN.

| | Fd1 (tsl1009) | Fd2 (tlr1236) | Fd1' | FdN (all4148) |
|---|---|---|---|---|
| $E_m$ (*vs* NHE)[a] | −372 ± 3 mV | −440 ± 13 mV | −344 ± 1 mV | −384 ± 9 mV |
| Experimental Mass | 10,714.45 Da | 11,729.5 Da | | 10,697.9 Da |
| (Native mode) | (10,889.12 Da) | | (10,921.28 Da) | |
| Calculated Mass | 10,715.8 Da | 11,730.3 Da | | 10,698.7 Da |
| Theoretical pI[b] | 3.93 | 5.45 | | 3.95 |
| *g* values g1/g2/g3 | 2.049/1.956/1.888 | 2.051/1.964/1.869 | 2.030/1.948/1.926 | 2.049/1.957/1.885 |
| Rhombicity ($Fd_{red}$)[c] | 85 | 106 | 35 | 84 |
| Spin delocalisation[c] | 23 | 23 | 29 | 23 |
| χvalues | 0.068 | 0.095 | 0.022 | 0.072 |
| Fd reduction by PSI | | | | |
| 1st order | sub-µs, 31–36 µs | 140 µs | sub-µs | |
| 2nd order[d] ($M^{-1} s^{-1}$) | (2.7 ± 0.5) × $10^8$ | (0.8 ± 0.1) × $10^8$ | - | |
| $K_d$ (µM) | 0.5 | 1.84 | 1.32 | |
| [PSI-Fd]↔[PSI] + [Fd] | | | | |

[a] The data are the average of results from titration curves in reduction and oxidation (see Supp. Fig. 2C). The data were fitted with Nernst curves with n = 1. $R^2$ values in the fitting procedure were ≥ 0.99 for all samples.
[b] Calculated on https://web.expasy.org/cgi-bin/compute_pi/pi_tool.
[c] According to Blumberg and Peisach [62] with the rhombicity = 300(($g_y$-$g_x$) / (2$g_z$-$g_y$-$g_x$)) and the spin delocalisation = 4/3(1/($g_z$-$g_x$) + 1/($g_z$-$g_y$)).
[d] The 2nd order rate constant was measured when the terminal acceptor ($F_A$ $F_B$) of PSI was singly reduced (after a single turnover flash) and when the Fd was oxidized.

### 3.3. EPR spectroscopy

The EPR spectra of reduced Fd1 and FdN are very similar, while the spectrum of Fd2 is slightly more rhombic and that of Fd1' is significantly more axial (Fig. 1B). The corresponding *g* values and the degree of rhombicity calculated as reported in [62] are given in Table 2. In reduced Fds, the $Fe^{2+}$ is localized on one of the irons, Fe1, and the variation in rhombicity of the EPR spectra has been interpreted in terms of distortion of the $Fe^{2+}$ tetrahedral environment, which results in variable mixing of some d orbitals of the $Fe^{2+}$ ion [63]. The value $\chi = g_2$-$g_3$ is correlated with the mixing between the $dz_2$ and the $dx_2$-$y_2$ orbitals allowed by the rhombic geometry. In addition, the width of the $g_3$ band, correlated with χ, was associated to the stiffness of the [2Fe−2S] site [63]. The χ values obtained for Fd2, Fd1, and Fd1' (χ = 0.095, χ = 0.068, and χ = 0.022, respectively) suggest a larger stiffness of the [2Fe−2S] cluster in Fd1' as compared to Fd1 or Fd2. A smaller χ value, as observed for Fd1' and to a lesser extent for Fd1 when compared to Fd2, has also been associated to a stronger antiferromagnetic exchange interaction between the two high spin irons of the [2Fe−2S] cluster [63]. Cys to Ser mutation of one of the Cys ligands of Fe2 in FdN has been found to lead to an axial EPR spectrum and to a splitting of the 330 nm band, which show similarities with the spectral characteristics of Fd1' [64], suggesting that the post-translational modification in Fd1' could affect the environment of the Fe2 iron.

### 3.4. Redox potentials

The redox midpoint potentials of the Fds were determined by spectro-electrochemical titrations at equilibrium in the UV–Vis range (Table 2, Supp. Fig. 2). The midpoint potential of FdN, −384 ± 9 mV, is in full agreement with the literature [65]. The mid-point potential of Fd1, −372 ± 3 mV, is close to that of FdN, and the midpoint potential of Fd1' is slightly less negative, by 28 mV. Fd2 has a significantly lower redox midpoint potential than Fd1, at −440 ± 13 mV. For Fd2, a small hysteresis possibly due to slow dynamics of Fd exchange at the electrode led to differences in the reductive and oxidative titrations. However, this hysteresis was much smaller than the ≈ −70 mV difference between the midpoint potentials of Fd2 and Fd1 (Supp. Fig. 2).

### 3.5. Crystal structure of Fd2

A thin plate crystal of Fd2 with a size of 130 µm × 50 µm × 10 µm (Supp. Fig. 3) was used to collect the X-ray diffraction data. The crystal belongs to the space group $P2_1$ with unit cell dimensions of $a$ = 28.0 Å, $b$ = 51.1 Å, $c$ = 31.6 Å (Supp. Table 1). The phase information was obtained by the molecular replacement method using the structure of Fd1 as the search model (PDB ID: 5AUI [21]), and the structure was refined to a resolution of 1.38 Å with $R_{work}$ and $R_{free}$ values of 0.1124 and 0.1570. For comparison, the structure of Fd1 from the same cyanobacterium was also determined to a resolution of 1.55 Å.

The structure of Fd2 contains residues 2–108 (the full length of the protein is 108 residues), a [2Fe−2S] type iron-sulfur cluster, a tentatively assigned sulfate ion, and 109 water molecules (Fig. 2A). The secondary structure of the domain contains three α-helices: α1, Ile33-Ala39; α2, Pro75-Asp79; α3, Glu101-Leu105, one $3_{10}$ helix: G1, Leu85-Ala87, and seven β-strands: β1, Val9-Asn16; β2, Leu21-His28; β3, Ala57-Lys62; β4, Val65-Gln67; β5, Phe82-Leu84; β6, Ala88-Pro90; β7, Cys94-Ser97. Five of the β-strands are arranged into a β-sheet with the strand order of β2-β1-β7-β3-β5 in an antiparallel fashion, except β1 and β7. The β-strands β4 and β6 are arranged antiparallel and connected to the main β-sheet with an angle almost perpendicular to it (Fig. 2A). The sulfate ion is probably needed for the crystal packing to fix the flexible N terminal loop structure by interaction with the loop structure, Gln67-Lys74. The electron density map at high resolution shows multiple conformations for amino acid side chains in some regions, in particular Val65, Asp66, Ser68, Asp69 and His70 as well as Val83, Cys94, and Ser97 (Supp. Fig. 4).

The iron and sulfur atoms in the [2Fe−2S] cluster are clearly located in the Fd2 structure based on their $2F_o$ - $F_c$ maps (Fig. 2B). The $mF_o$ - $DF_c$ map showed some weak negative densities around the center of the cluster (Fig. 2C), possibly caused by some X-ray irradiation damage during data collection, as the [2Fe−2S] cluster is very prone to radiation damage. As expected from the sequence alignment (Table 1), Cys48, Cys53, Cys56, and Cys86 are involved in the coordination of the cluster (Fig. 2B and C). Cys48 and Cys53 are coordinated to the iron atom Fe1, and Cys56 and Cys86 to Fe2. The [2Fe−2S] cluster is located near the surface of the molecule and Fe1 and the sulfur atoms of Cys48 and Cys53 face the solvent. The bond lengths and angles among the iron-sulfur cluster atoms of Fd2 and Fd1 are summarized in Table 3. Bond lengths are in line with typical bond lengths of 2.30 Å and 2.24 Å reported in the literature between the iron and the Sγ atoms of the cysteine residues, and between the iron and bridging sulfur atoms of the [2Fe−2S] cluster, respectively [6].

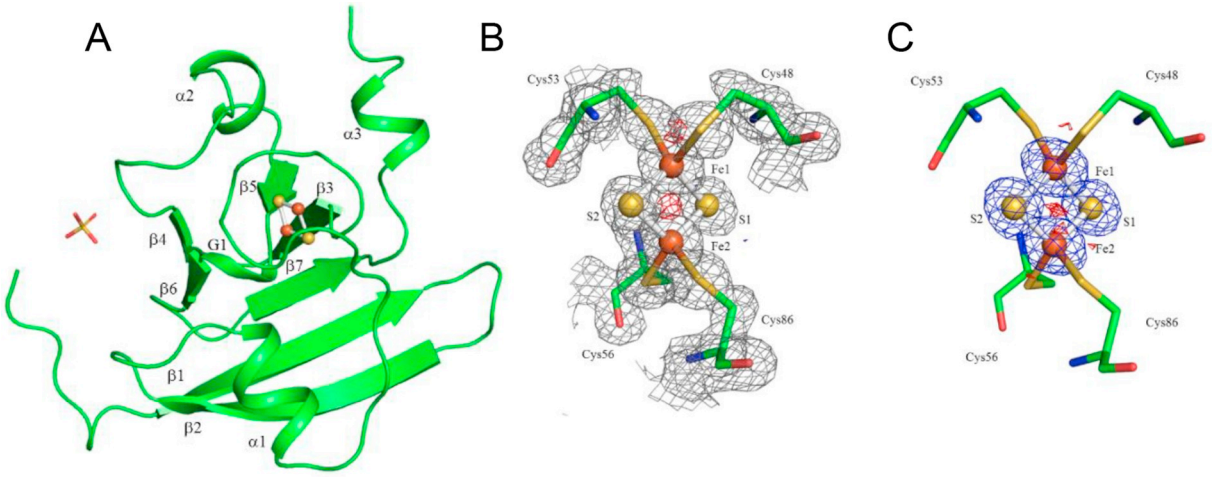


**Fig. 2.** Crystal structure of an alternative [Fe−2S] ferredoxin, Fd2 coded by *tlr1236* in *T. elongatus*.
(A) Ribbon model of the whole structure. The crystal structure contains residues 2–108 (the full length of the protein is 108 residues), a [2Fe−2S] type iron-sulfur cluster (shown in ball), and a tentatively assigned sulfate ion (shown in stick). The color of the Fd2 structure is in green and iron atoms are in brown, and sulfur and oxygen atoms of the sulfate iron are shown in yellow and red, respectively. Secondary structures of Fd2 were shown as follows: α, α-helix; G, $3_{10}$ helix; β, β-strand. (B) Iron-sulfur cluster in the Fd2 structure of *T. elongatus*. Final σ-weighted $2mF_o$ - $DF_c$ electron density map around the cluster contoured at a 1.0 σ level shown in grey. Positive and negative electron densities derived from $mF_o$ - $DF_c$ electron density map are contoured at a 3.5 σ level and shown in blue and red, respectively. (C) Omit map for the iron sulfur cluster at a 3.5 σ level. Positive and negative electron densities are shown in blue and red, respectively.

**Table 3**
Bond lengths and angles among atoms related to the iron-sulfur cluster.

| | Fd2 (Å) | Fd1 (Å) | Fd1[a] (Å) |
|---|---|---|---|
| FE1-Cys48[b] Sγ | 2.28 | 2.31 | 2.31 |
| FE1-Cys53[b] Sγ | 2.25 | 2.31 | 2.34 |
| FE2-Cys56[b] Sγ | 2.26 | 2.28 | 2.32 |
| FE2-Cys86[b] Sγ | 2.30 | 2.31 | 2.30 |
| FE1-S1 | 2.25 | 2.22 | 2.30 |
| FE1-S2 | 2.19 | 2.24 | 2.26 |
| FE2-S1 | 2.19 | 2.25 | 2.24 |
| FE2-S2 | 2.16 | 2.11 | 2.24 |
| FE1-FE2 | 2.72 | 2.71 | 2.79 |
| S1-S2 | 3.45 | 3.47 | 3.54 |
| S1-Ser47[c] N | 3.32 | 3.24 | 3.21 |
| S1-Cys48[c] N | 3.55 | 3.43 | 3.52 |
| S1-Arg49[c] N | 3.19 | 3.28 | 3.32 |
| S2-Ala52[c] N | 3.46 | 3.44 | 3.46 |
| S2-Cys53[c] N | 3.32 | 3.43 | 3.31 |
| S2-Cys53[c] O | 3.27 | 3.27 | 3.13 |
| Cys48[b] Sγ-Arg49[c] N | 3.22 | 3.31 | 3.34 |
| Cys48[b] Sγ-Ala50[c] N | 3.24 | 3.30 | 3.27 |
| Cys48[b] Sγ-Ala52[c] N | 3.39 | 3.45 | 3.49 |
| Cys53[b] Sγ-Val54[c] N | 3.32 | 3.36 | 3.33 |
| Cys53[b] Sγ-Asn55[c] N | 3.32 | 3.44 | 3.36 |
| (Cys46[b] Sγ- Ser40 OG in Fd1) | – | 3.04 | – |
| (Cys46[b] Sγ-Thr48 OG in Fd1) | – | 3.36 | 3.36 |
| Cys56[b] Sγ-Leu85[c] N | 3.41 | 3.43 | 3.41 |
| Cys86[b] Sγ-Gly51[c] N | 3.36 | 3.54 | 3.49 |

| | Fd2 (°) | Fd1 (°) | Fd1[a] (°) |
|---|---|---|---|
| Cys48[b] Sγ-FE1-Cys53[b] Sγ | 105.63 | 104.61 | 105.66 |
| Cys56[b] Sγ-FE2-Cys86[b] Sγ | 106.06 | 106.29 | 105.72 |
| S1-FE1-S2 | 101.95 | 102.34 | 101.95 |
| FE1-S1-FE2 | 75.48 | 74.61 | 75.92 |
| FE1-S2-FE2 | 77.20 | 76.99 | 76.78 |
| S1-FE2-S2 | 104.77 | 105.68 | 104.45 |
| S2-Cys53[c] O-Cys53[c] C | 96.77 | 105.08 | 106.22 |

[a] PDBID: 5AUI [21].
[b] Cys48, Cys53, Cys56 and Cys86 in Fd2 correspond to Cys41, Cys46, Cys49 and Cys79 in Fd1, respectively.
[c] Conserved residues Ser47-Cys53 and Leu85 in Fd2 correspond to Ser40-Cys46 and Thr78 in Fd1.

### 3.6. Structural comparison of Fd2 and Fd1

The structures of the two [2Fe-2S] clusters in Fd1 (PDBID: 5AUI [21] and this work) and Fd2 are not significantly different, although the overall structures of Fd2 and Fd1 exhibit relatively large differences in several regions. These differences include an additional N-terminal structure, Thr2-Asn7 in Fd2, two loop regions defined as loops 1 and 2, the α2-helix adjacent to loop 2, and the C-terminal region (Fig. 3A–B, Supp. Fig. 5).

On a global scale, the distribution of surface charges and the properties of the dipole moment are significantly different for Fd1 and Fd2 (Fig. 3C–E). The surface charges are close to neutrality at the iron-sulfur center for Fd1 and Fd2. In contrast, the specific N-terminal extension and the loop 2 structure of Fd2 not only modify the overall shape of the protein but also result in a more positive surface charge distribution in this area than for Fd1. The magnitude and orientation of the dipole moment in Fd2, calculated as previously described [51], completely differs from that of Fd1 in which the dipole moment is close to that observed for other Fd1-type cyanobacterial Fds for which a 3D-structure has been reported (Fig. 3E, data collected in Supp. Table 2). Remarkably, Fd2 has a small net charge of −6, *versus* −17 on average for the Fd1-type Fds. The magnitude of the dipole moment in Fd2, in both the oxidized and reduced states, is also larger than in Fd1-type Fds. Although the dipole moment in the heterocyst Fd from *Nostoc* PCC7120 has also a large magnitude, its orientation is very different from those of both Fd1 and Fd2 (Fig. 3E).

At the atomic scale, differences are noticeable between Fd1 and Fd2 in loop 1 and loop 2 and more generally in the hydrogen bonding interactions and orientation of key residues. The differences in loop 1 (Asn16-Leu21 of Fd2 or Arg9-Ser13 of Fd1) include the deletion of one amino acid in Fd1 as compared to Fd2 and the replacement of Pro11 in Fd1 by Glu17 in Fd2. This induces local differences in hydrogen bond patterns (Supp. Fig. 6). Larger structural differences are observed for loop 2 (Gln67-Lys74 in Fd2 or Gln60-Asp67 in Fd1, Supp. Fig. 7), with consequences on hydrogen bonding interactions involving the loop around the [2Fe−2S] cluster (Fig. 4). The amino acid sequences are not much different but the loop 2 structures are quite different. These differences are caused by the bulkiness of His70 in Fd2 compared with Gln63 in Fd1, and by the very different orientation of the conserved phenylalanine side chain Phe72 in Fd2 as compared to Phe65 in Fd1.

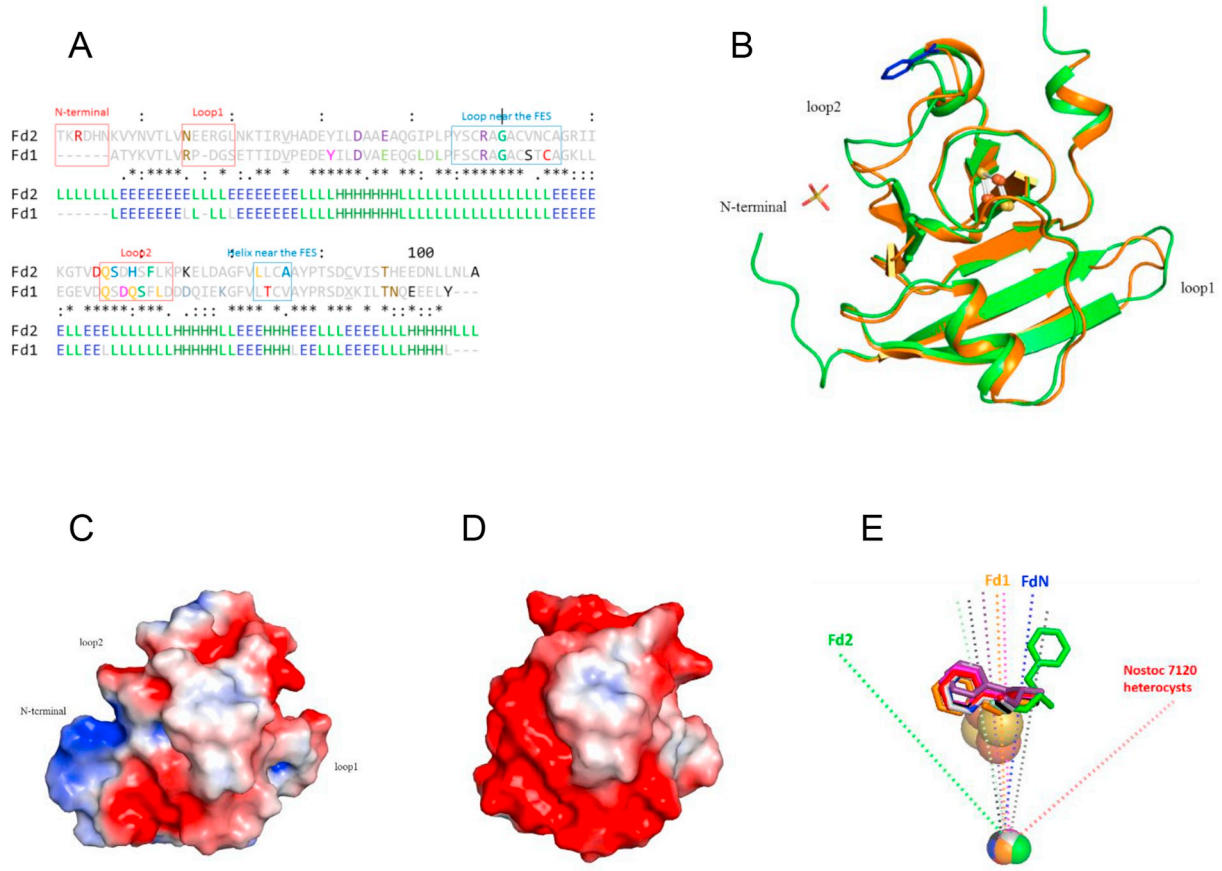


**Fig. 3.** Comparison of Fd2 and Fd1 structures

(A) Sequence alignment of Fd1 (coded by the *tsl1009* gene) and Fd2 (coded by the *tlr1236* gene). The first and second lines show the alignment of the amino acid sequences of Fds derived from PDB structures. The conserved cysteine residues except the cysteine ligands of the [2Fe−2S] cluster are shown in underbars (X in Fd1 (PDBID: 5aui [21]) means CSO which is *S*-hydroxycysteine). Red frames show the N terminus, loop 1 and loop 2 whose structures are different in Fd2 and Fd1. Blue frames show the loop and helix regions near the [2Fe−2S] cluster (FES). Residues interacting through hydrogen bonds are shown with the same color. The first residue of Fd2 (Thr) is numbered 2 in the Fd2 pdb structure whereas the first residue in Fd1 (Ala) is numbered 1 in the Fd1 pdb structure. The third line highlights the similarity of amino acids between Fds. The symbols used are as follows: "*" (asterisk) indicates fully conserved residues; ":" (colon) and "." (period) indicate conservations between groups of strongly similar properties – scoring > or ≤0.5 in the Gonnet PAM 250 matrix, respectively; "-" indicates the absence of residues. The score for the similarity between different Fds was 53.1. The fourth and fifth lines show the secondary structure assignments of Fds performed by DSSP [101,102]. *H*, helix; *E*, strand; *L*, coil.

(B) Structure comparison between Fd2 (green) and Fd1 (PDB ID: 5aui [21], orange for the protein body and blue for the benzamidine ligand). The iron sulfur clusters in Fd2 and Fd1 are drawn in a ball model. The structures of Fd2 and Fd1 of *T. elongatus* were superimposed using the SSM method.

(C and D) Surface charge distributions of Fd2 (C) and Fd1 (D, PDB ID: 5aui). The structures are shown with the same orientation as in panel B. Blue and red represent positive and negative areas, respectively. The areas surrounding the iron sulfur cluster are mostly charge neutral, which is shown in white.

(E) Orientation of the dipole moments of ferredoxins from cyanobacteria. All structures from cyanobacterial Fds (references given in Supp. Table 2) were aligned with PyMol (using α carbons). The [2Fe−2S] clusters were found almost perfectly superimposed after alignment. For clarity, only the Fd2 [2Fe−2S] cluster is shown. The lines correspond to the dipole vectors. They are traced from the centers of mass of each protein, with an equal length of 20 Å. Identification of the dipoles from left to right: *T. elongatus* Fd2 (green), *Syn*. 6803 (pale green), *Leptolyngbya boryana* (black), *Arthrospira platensis* (purple), *T. elongatus* Fd1 (orange), *Aphanothece sacrum* (magenta), *Nostoc* PCC7119 FdN (blue), *Mastigocladus laminosus* (grey), *Nostoc* 7120 heterocyst Fd (red). The orientation of the conserved Phe72 (Fd2 numbering) in the different structures is also displayed with the same color coding.

The specific orientation of Phe72 in Fd2 in turn results from the bulkiness of the Val54 residue in the $Cys_{53}ValAsnCys_{56}$ sequence of Fd2, as compared to the Ser47 side chain in the corresponding $Cys_{46}SerThrCys_{49}$ sequence of Fd1 (Fig. 4C). The different loop 2 structures are also due to different hydrogen bonding patterns derived from the different amino acids present in the Leu51-Lys73 sequence for Fd1 or Arg59-Ala80 sequence in Fd2 (Supp. Fig. 7). In addition, in Fd2, residues Asp66 and Lys76 near loop 2 have interactions with residues Arg4 and Ala108 of the N- and C- terminus, respectively, which have no equivalents in Fd1 (Fig. 4A).

Some hydrogen-bond connections to the [2Fe−2S] clusters are also different in Fd1 and Fd2 (Fig. 4C and Table 3). The hydrogen bond between Cys46/Sγ ligand of Fe1 and Thr48/Oγ is specific of the $Cys_{46}Ser_{47}Thr_{48}Cys_{49}$ motif of Fd1 (Fig. 4C). The bond angle and distance between the bridging S2 and the Cys53 peptide carbonyl C═O (corresponding to Cys46 in Fd1) are slightly different between Fd1 and Fd2, as well as the hydrogen bonding distances between S1 and the peptide NH groups of Ser47 and Arg49. The distances between Cys48/Sγ and the peptide groups of Arg49, Ala50 and Ala52 are slightly shorter in Fd2 as compared to Fd1 (Table 3). The distance Cys86Sγ-Gly51N is also shorter in Fd2. These differences probably result in part from different interactions formed by the side chains of Arg49 and Arg42 in Fd2 and Fd1, respectively (Fig. 4A–B).

Other significant differences in hydrogen bonding connections are present in some regions of the two Fds. The hydrogen bond of Gly51 with Phe72 in Fd2 is replaced by an H-bond between the homologous Gly44 and Ser64 in Fd1 (Fig. 4C). The interaction between Ser68 and Ala87 is observed only in Fd2 (Fd2 numbering), while hydrogen-

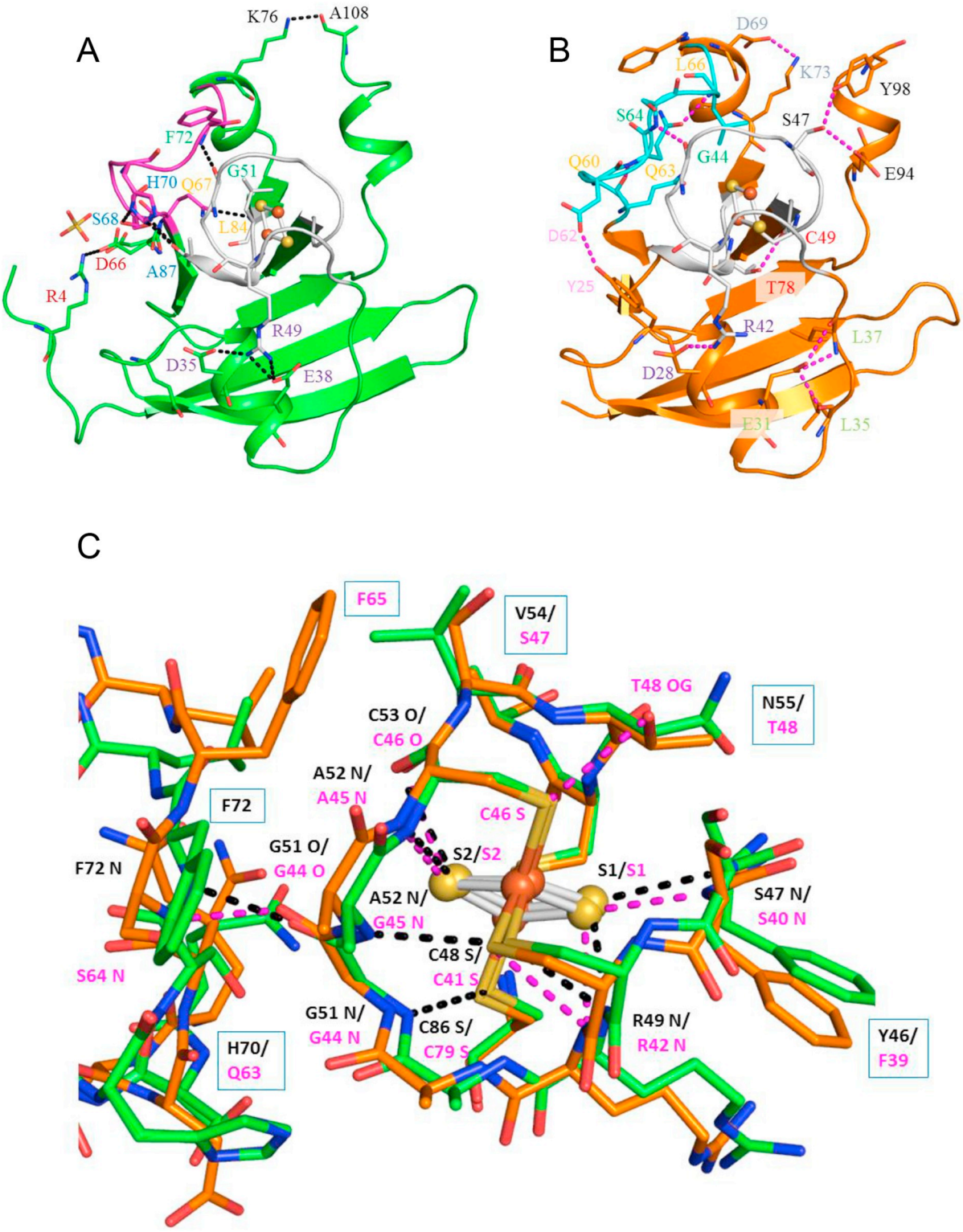


**Fig. 4.** Hydrogen bond connections on the loops near the iron clusters.
The residues involved in hydrogen bonds in the regions near the [2Fe–2S] cluster are shown as sticks in the structures of Fd2 (A) and Fd1 (PDB ID: 5aui [21]) (B). Loop 2 and the regions near the [2Fe–2S] cluster are shown in purple (Fd2) or blue (Fd1) and light grey. Dashed lines, black for Fd2 and magenta for Fd1, indicate hydrogen bonds between the residues. The characters of residues, which are in hydrogen bonding interaction, are shown in the same color as in Fig. 3A. (C) Hydrogen bonds among the residues located in the loop near the iron sulfur cluster and in loop 2 region. The residues are shown in stick model with the same color as in Fig. 3B, in addition to blue color for the nitrogen atoms. Hydrogen bonds which lengths are < 3.4 Å are shown in dashed line with black and magenta for Fd2 and Fd1, respectively. The residues, which are different or differently oriented in the different Fds are indicated in frames (see Table 3 for the lengths of bonds involving the sulfur atoms).

bonding interactions between Tyr25 and Asp62, Glu31 and Leu35, Cys49 and Thr78, and between Ser47, Glu94 and Tyr98 are observed only in Fd1 (Fd1 numbering, Fig. 4B). These different connections seem to be caused by the differences in amino acid residues Pro43Asp, Tyr46Phe, Val54Ser and Asn55Thr in the CysValAsnCys (Fd2) or CysSerThrCys (Fd1) motifs, as well as His70Gln, Leu85Thr and Ala87Val, or orientation differences such as those of Arg49 and Phe72, between Fd2 and Fd1 (Fd2 numbering).

The structural properties of Fd2 are thus very different from previously reported Fds structures from cyanobacteria both at the global and molecular or atomic scale. These differences will be further discussed in relation with the redox and electron transfer properties of Fd1 and Fd2.

### 3.7. Vibrational properties determined by FTIR difference spectroscopy

Structural differences between Fd1 and Fd2 and structural changes associated to the redox changes of the [2Fe−2S] cluster were also identified using FTIR difference spectroscopy coupled with electrochemistry in the mid- and far- infrared regions. The Mid-IR range gives information on protein conformation and on amino acid side-chain modes, while the metal-ligand signatures of the [2Fe−2S] center are contributing in the Far-IR domain.

In the Mid-IR range, the reduced-*minus*-oxidized spectra recorded with all the Fds are dominated by contributions from peptide $\nu$(C=O) Amide I and $\nu$(CN) + $\delta$(NH) Amide II vibrational modes at 1700–1620 $cm^{-1}$ and 1550–1500 $cm^{-1}$, respectively (Fig. 5), as shown by $^{1}H_2O/^{2}H_2O$ exchange experiments (detailed in Supp. Fig. 8). These bands correspond to a minute reorganization of the protein backbone both on the active site loop and on the β-sheet structure. Contributions from β-sheet structures are inferred from the band at 1642–1638 $cm^{-1}$ ($Fd_{red}$) and those from loops or α-helices from bands at 1668–1672 ($Fd_{ox}$) and 1653–1649 $cm^{-1}$ ($Fd_{red}$) [66]. The band at 1700–1692 $cm^{-1}$ ($Fd_{ox}$) corresponds to carbonyl group(s) free of hydrogen bonding interactions. These amide bands probably result in part from changes in the strength of hydrogen bonding interactions between the Cys ligands of the [2Fe−2S] cluster and peptide carbonyl groups upon Fds reduction.

Spectra recorded with Fd1 and FdN are strikingly similar, not only in the amide range but also in a fingerprint region below 1400 $cm^{-1}$, where mainly amino acid side-chain modes are expected to contribute (Fig. 5). This indicates very similar structural reorganization upon [2Fe-2S] oxidation/reduction in Fd1 and FdN and similar redox-sensitive amino acids. The spectrum obtained with Fd1' is also highly similar to that of Fd1 in the 1800–1000 $cm^{-1}$ range. Small redox-sensitive structural differences between Fd1 and Fd1' are observed at the level of a loop and/or α-helix with a Fd1' upshift by ≈1 $cm^{-1}$ of the band at 1668/1653 $cm^{-1}$ and differences in the relative amplitude of bands at 1566, 1551, 1528 and 1522–1520 $cm^{-1}$ [66].

The FTIR difference spectra recorded with Fd1 and Fd2 in $H_2O$ and in $^{2}H_2O$ (Fig. 5 and Supp. Fig. 8) present an overall similarity, although significant differences are observed both in the Amide I and Amide II regions as well as below 1400 $cm^{-1}$. Bands at 1668, 1652 and 1640 $cm^{-1}$ in Fd1 appear upshifted by 1–4 $cm^{-1}$ in Fd2 and the band at ≈1698 $cm^{-1}$ is more clearly split into two contributions at 1692 and 1705 $cm^{-1}$ for $Fd2_{ox}$. Different frequencies are also observed in the Amide II range for $Fd2_{red}$ at 1554 and 1525 $cm^{-1}$ in $H_2O$ and at 1433 and 1406 $cm^{-1}$ in $^{2}H_2O$ for $Fd2_{ox}$ (Supp. Fig. 8). These spectral differences point to slightly different properties of the peptide bonds and notably of the β-sheet structure in Fd2 or of their minute reorganization upon reduction. The frequency of amide carbonyl groups from β-sheet structures has been correlated to the β-sheet twist angle δ [67–69]. The slightly higher frequency observed at 1642 $cm^{-1}$ for Fd2 suggests a very small increase in this twist angle δ in Fd2.

The effect of $^{1}H_2O/^{2}H_2O$ exchange also suggests contributions from side-chains of tyrosine, aspartate and/or glutamate in the

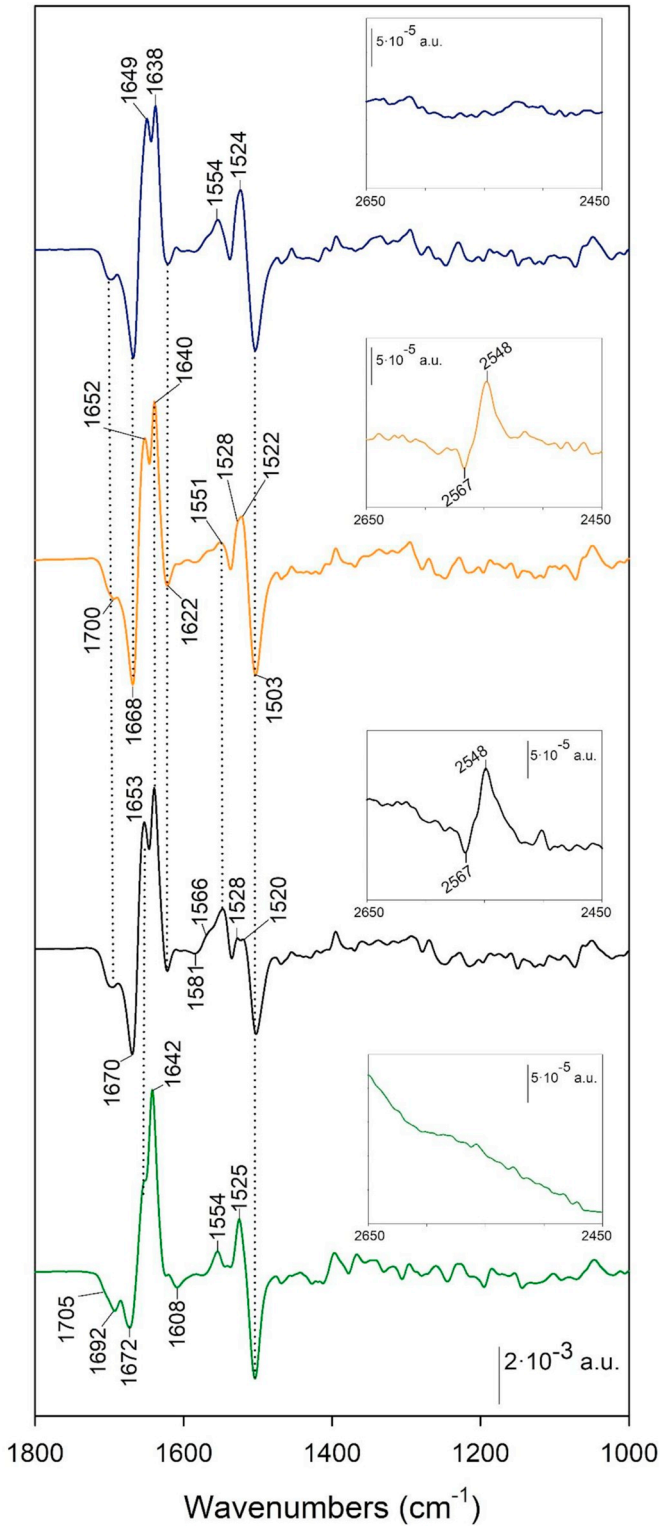


**Fig. 5.** Reduced-*minus*-oxidized FTIR difference spectra in the mid-IR. Spectra recorded with FdN (blue line), Fd1 (orange line), Fd1' (black line) and Fd2 (green line).

1576–1504 $cm^{-1}$ range, which show different frequencies for Fd1 and Fd2 (Supp. Fig. 8A). In addition, below 1400 $cm^{-1}$, bands at 1295/1279 $cm^{-1}$ and at 1074–72/1063 $cm^{-1}$ observed for Fd1, Fd1' and FdN but not for Fd2 are tentatively assigned to a redox-sensitive Thr or Ser side-chain (Supp. Fig. 8B). They are therefore proposed to arise from the $Cys_{46}SerThrCys_{49}$ motif in direct interaction with the [2Fe−2S]

cluster, which is not conserved in Fd2.

Surprisingly, a band shift from 2567 $cm^{-1}$ to 2548 $cm^{-1}$ is observed for Fd1 and Fd1' but not for FdN or Fd2 (Fig. 5 insets). This band is characteristic of the ν(SH) mode of a cysteine side chain [70] and the −19 $cm^{-1}$ downshift upon Fd1 reduction indicates a stronger hydrogen bonding interaction in reduced Fd1. This band could be due to Cys87 not involved in coordination of the [2Fe−2S] cluster in Fd1, since this cysteine has no equivalent in FdN. The Cys87 side-chain is at hydrogen bonding distance to the carbonyl oxygen of Glu57 in our new Fd1 structure (3.14 Å, Supp. Fig. 9, the structure PDBID: 5AUI [21] has a Cys-SOH group at this position). The ν(SH) band is not detected for Fd2, although the Cys is conserved (Cys94) and at hydrogen bonding distance to the carbonyl oxygen of Thr64 (3.05 Å, Supp. Fig. 9). Since two electron densities are observed for the Cys94 side chain in the Fd2 structure, as well as for residues Val65-His70 located just after Thr64 (see above), some flexibility probably exists in this region that could impair the formation of a strong hydrogen bond and explain the absence of a ν(S−H) band in the FTIR spectrum. Alternately, the ν(S−H) band may result from a specific interaction between the Cys46 ligand of the [2Fe−2S] cluster and Ser40 and Thr48 in Fd1, as revealed in the new Fd1 structure (Supp. Fig. 10 and descriptions of the new Fd1 structure in Supp. Fig. 11). In this structure, in addition to a conformation involving an hydrogen bonding interaction between Ser40 and Glu31 from the adjacent molecule, as reported in [21] and probably caused by crystal packing, we observe a second conformation of Ser40 in interaction with Cys46 and Thr48 (Supp. Fig. 10B). This later conformation likely represents the structure in solution without the effect of crystal packing. Proximity between Cys46 and Ser40 was not found in FdN in spite of their similar amino acid sequences. This is probably due to the different orientations of Arg42 and Phe39 between Fd1 and FdN, which brings the backbone of Ser41 in FdN closer to the [2Fe−2S] cluster and forces Ser41-OG orientation toward outside of the cluster (Supp. Fig. 10B). In Fd2, the orientation of Ser47-OG is also different, because Thr48 in Fd1 is replaced by Asn55, in Fd2. Thus we cannot exclude that the ν(S−H) IR mode may account for a protonated Cys46-Sγ stabilized by a strong and specific hydrogen bonding interaction with the Ser40-OG in Fd1.

In the Far-IR range, the spectra recorded with FdN and Fd1 are almost identical both in shape and in band frequencies, except for a difference band at 554/540 $cm^{-1}$ present only in Fd1 (Fig. 6, see band assignments in Table 4). The spectrum recorded with Fd2 has the same overall shape, but some bands appear at significant different frequencies. Above 450 $cm^{-1}$, far-IR bands are associated to contributions from the peptide –CO–NH– moiety (Amide IV-VI bands) and amino acid side-chains. We assign the main bands at 581 and 507 $cm^{-1}$ for $Fd1_{ox}$ and $FdN_{ox}$ to Amide IV-VI modes associated to peptide bonds. The Amide IV-VI modes are very sensitive to the peptide bond properties and conformation and are up-shifted upon hydrogen bond strengthening [71–73]. These bands appear at +11 and +6 $cm^{-1}$, respectively, for $Fd2_{ox}$, suggesting that the redox-sensitive peptide groups are involved in stronger hydrogen bonding interactions in Fd2 than in Fd1 or FdN.

The $Cys_4Fe_2S_2$ cluster contributes to bands below 450 $cm^{-1}$. The ν(Fe-Sb[3]) IR modes involving the bridging sulfurs are assigned at 423–424, 388–389 and 360 $cm^{-1}$ for $Fd1_{ox}$ or $FdN_{ox}$ (*i.e.* $B_{2u}$, $A_g$ and $B_{3u}$ modes, Table 4) and at 397–398, 380 and 311 $cm^{-1}$ for $Fd1_{red}$ or $FdN_{red}$, in agreement with the literature [74–77]. The large frequency downshift of the ν(Fe−Sb) modes upon Fd reduction is in line with structural data on FdN, which show that the largest change upon reduction of the [2Fe−2S] cluster is related with the Fe1−Sb distances and the positions of the Fe1 atom and S2 bridging sulfur [14].

The ν(Fe−Sb) mode frequencies are very similar for Fd1 and Fd2 both in the oxidized and reduced states (Table 4). This indicates almost similar properties of the Fe−Sb bonds in reduced and oxidized Fd1 and Fd2. In contrast, significant differences are observed between Fd1 (or FdN) and Fd2 for modes involving ν(Fe−St) contributions. The ν(Fe−St) mode contributes at 349 $cm^{-1}$ for $Fd2_{ox}$ ($B_{1u}$ mode, [75,76,78,79]) and at significantly higher frequency in $Fd1_{ox}$ or $FdN_{ox}$, as a shoulder at ~356 $cm^{-1}$, almost superimposed to the ν(Fe−Sb) mode at 360 $cm^{-1}$. For reduced Fds, the $B_{1u}{}^t$ and $B_{3u}{}^t$ modes involving ν(FeIII−St) and ν(FeII−St) vibrations, respectively [74] contribute at 321-320 and 278-276 $cm^{-1}$ for $FdN_{red}$ and $Fd1_{red}$, and at 316 and 270 $cm^{-1}$ for $Fd2_{red}$. The significantly lower ν(Fe−St) mode frequency for Fd2 in both the oxidized and reduced forms, points to weaker Fe−St interactions in Fd2 or different geometries of Fe-Cys bonds, since the ν(Fe−St) mode is coupled with the SCC bending mode of the cysteine ligand and this coupling depends on the Fe-S-C-C dihedral angle [74,80]. In addition, the effect of $^1H_2O/^2H_2O$ exchange on the ν(FeII−St) mode of reduced Fd is smaller and in opposite directions for Fd2 as compared to Fd1 (Table 4). A larger effect of $^1H/^2H$ exchange on the Raman bands of the $Cys_4Fe_2S_2$ cluster has been taken as indicative of stronger cluster

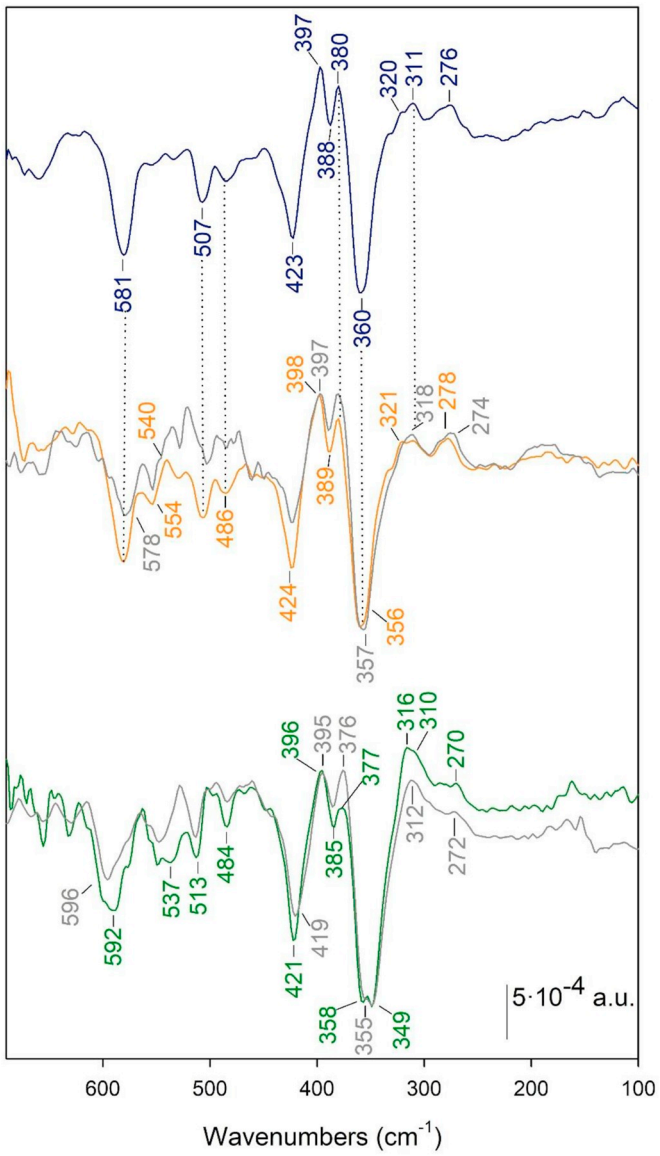


**Fig. 6.** Reduced-*minus*-oxidized FTIR difference spectra recorded in the Far-IR domain.
Spectra recorded with FdN (blue line), Fd1 (orange line in $H_2O$ and grey line in $^2H_2O$) and Fd2 (green line in $H_2O$ and grey line in $^2H_2O$).

[3] Sb stands for bridging sulfur of the [2Fe−2S] cluster, while St stands for terminal sulfur corresponding to CysSγ.

**Table 4**
Vibrational modes of the [2Fe−2S]$Cys_4$ active site of Fds in the Far-IR domain.

| FdN | | Fd1 | | Fd2 | | Proposed assignments |
|---|---|---|---|---|---|---|
| Ox | Red | Ox | Red | Ox | Red | |
| 581 | | 581 (−3) | | 592 (+4) | | Amide IV-VI modes |
| | | 554 | 540 | | | |
| | | 529 (−1) | | 537 | | |
| 507 | | 507 (−5) | | 513 (0) | | |
| 486 | | 486 | | 484 (0) | | |
| 423 | 397 | 424 (0) | 398 (−1) | 421 (−2) | 396 (−1) | $B_{2u}{}^{b}$ ν(Fe−Sb) |
| 388 | 380 | 389 (0) | 380 (0) | 385 (0) | 377 (−1) | $A_{g}{}^{b}$ ν(Fe−Sb) |
| 360 | 311 | 360 (−3) | 311 (0) | 358 (−3) | 310 (0) | $B_{3u}{}^{b}$ ν(Fe−Sb) |
| 356 (sh) | | 356 (sh) | | | | |
| 356 (sh) | 320 | 356 (sh) | 321 (−3) | 349 (0) | 316 (−4) | $B_{2g}{}^{t}/B_{1u}{}^{t}$ ν(FeIII−St) |
| | 276 | | 278 (−4) | | 270 (+2) | $B_{3u}{}^{t}$ ν(FeII−St) |

Numbers under brackets correspond to the frequency shift in $^{2}H_2O$. The absence of numbers indicates that the corresponding band in $^{2}H_2O$ was ambiguous. Assignments are proposed by reference to literature data [74,76]. Amide IV-VI modes involve in plane and/or out of plane CO bending modes, CC stretch motions, together with CNC deformation and NH out of plane bending modes of the peptide CO-NH bond. Sh: shoulder

interaction with the peptide moiety of the protein [74,77].

The Far-IR data thus show that main differences between Fd1 (or FdN) and Fd2 concern the interactions between the [2Fe−2S] cluster and the cysteine ligands both in the oxidized and reduced states. These data are in line with the structural data for the oxidized proteins.

### 3.8. Kinetics of Fd reduction by photosystem I

Electron transfer kinetics from PSI to Fds were compared for Fd1, Fd2 and Fd1' from *T. elongatus*. Photoinduced charge separation and stabilization in PSI lead to the formation of the state $P700^{+}$-$(F_A\ F_B)_{1red}$ within a few hundreds of nanoseconds ($(F_A\ F_B)_{1red}$ = singly reduced ($F_A\ F_B$)).[4] $F_B$ is the direct partner of Fd during forward electron transfer (ET). The kinetics of Fd reduction by $F_B{}^{-}$ have submicrosecond and microsecond phases in the first-order kinetics that correspond to Fd bound to PSI prior to the laser flash illumination and a slower second-order [Fd]-dependent phase that corresponds to Fd reduction preceded by diffusion-limited binding of Fd to PSI.

The kinetics of Fd reduction have long been studied by flash-absorption spectroscopy with PSI and Fd from the cyanobacterium *Syn.* 6803 [52,81] and more recently, in *T. elongatus* [51,82]. The present measurements were performed at 580 nm, a wavelength where Fd reduction by $(F_A\ F_B)_{1red}$ results in a decrease in the absorption. The dissociation constant $K_d$ of the PSI:Fd complex "at rest", *i.e.* with the terminal PSI acceptor ($F_A\ F_B$) and Fd both oxidized, the first-order ET rate(s) and the second-order kinetics of $Fd_{ox}$ reduction by PSI are given in Table 2. Several differences are observed between the three Fds.

First, the $K_d$ values of Fd2 (1.84 μM) and of Fd1' (1.32 μM) are ~3 times larger than that of Fd1 (0.5 μM) (Supp. Fig. 13). The present value of $K_d$(Fd1) is slightly smaller than the value of 0.76 μM recently determined [51]. This is very likely due to the use of different preparations of PSI trimers, since $K_d$ values from 0.2 to 0.8 μM were reported for different preparations of PSI trimers from *Syn.* 6803 [52]. In the present work, the same PSI preparation was used for comparing Fd1 and Fd2 whereas Fd1' was studied with another PSI preparation.

Second, the first-order intracomplex ET kinetics (Fig. 7, series of Fd2 kinetics in Supp. Fig. 12) significantly differ with the three Fds. These kinetics were obtained by subtracting the signal recorded with PSI alone from those recorded with PSI and the different Fds (original kinetic data and $K_d$ titration curves in Supp. Figs. 12–13). With Fd1, a kinetically non-resolved sub-μs component appearing as a step-like

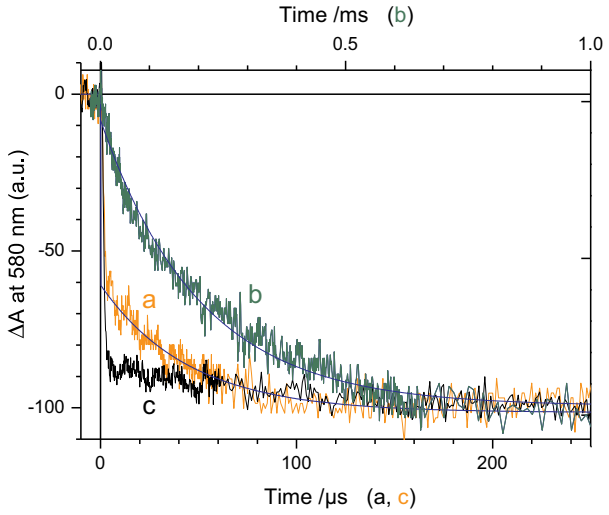


**Fig. 7.** Kinetics of electron transfer between reduced PSI and ferredoxins Fd1, Fd2 and Fd1'.
The negative signals attributed to intracomplex first-order Fd reduction are normalized to (−100) so as to easily compare their kinetics. The time scale for Fd1 (trace a, orange) and Fd1' (trace c, black) is at the bottom where that for Fd2 (trace b, green) is at the top. Traces a and b were fitted by monoexponential decay functions with $t_{1/2}$ of 31 μs and 140 μs, respectively (blue traces). These kinetics reflect Fd reduction by $(F_A\ F_B)_{1red}$ within PSI:Fd complexes which are preformed before flash excitation.

negative signal and a component with a $t_{1/2}$ of ~33 μs are observed. The presence of only one μs component, instead of two in a previous report [51] has no consequences on the interpretation of the present data. Reduction kinetics of Fd1' are mostly in the sub-μs range with possibly a minor μs component, while with Fd2 no sub-μs component is present and the sub-ms decay kinetics can be fitted with a single phase with a $t_{1/2}$ of 140 μs. The midpoint potentials of the different Fds increase from Fd2 to Fd1 to Fd1' (Table 2). Therefore, it appears that the rates of intracomplex Fd reduction increase with the driving force for ET from $(F_A\ F_B)_{1red}$ to $Fd_{ox}$, as expected.

Third, the association rate constant $k_{on}$ obtained from the second-order kinetics is ~3-fold smaller for Fd2 ($0.8 \pm 0.1\ 10^{8}\ M^{-1}\ s^{-1}$; Supp. Fig. 12) than for Fd1 ($2.7 \pm 0.5\ 10^{8}\ M^{-1}\ s^{-1}$) [51]. This difference may be attributed to the differences in the global charges or protein dipoles between Fd2 and Fd1. $K_{on}$ could not be reliably determined in the case of Fd1', due to the lack of protein. Albeit these different kinetic properties, we can conclude that Fd2 can be efficiently reduced by PSI.

[4] P700 is a dimer of chlorophyll *a* molecules located on the lumenal side of the photosynthetic membrane. $F_A$ and $F_B$ are both [4Fe-4S] clusters in sub-μs redox equilibrium, borne by the PSI subunit PsaC, which is located on the cytoplasmic/stromal side of the membrane.

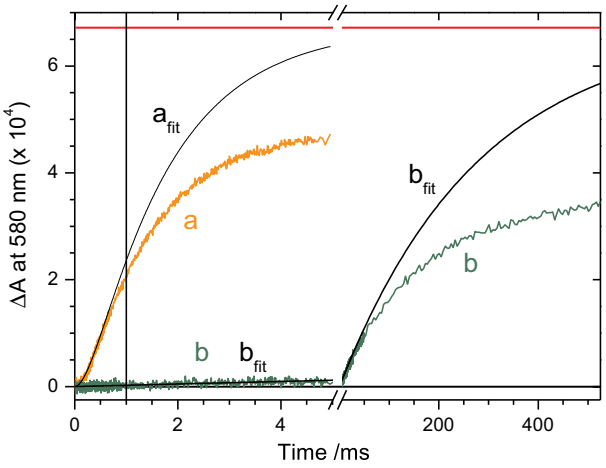


**Fig. 8.** Kinetics of FNR reduction by reduced Fd1 (trace a) and Fd2 (trace b) at pH 8.0.
The figure directly exhibits the kinetics of FNR reduction by $Fd_{red}$ as PSI contributions as well as Fd reduction kinetics are eliminated (see Methods). Trace a (orange) is obtained with Fd1 and trace b (dark green) is obtained with Fd2. PSI concentration was 0.20 μM whereas very similar concentrations of Fd and FNR were used in both cases (a: 3.86 μM Fd1 and 7.82 μM FNR; b: 3.88 μM Fd2 and 7.79 μM FNR). The red line indicates the signal size for full formation of $FNR_{sq}$ and reoxidation of $Fd1_{red}$. The signal sizes at 1 ms (vertical line) were found to be $2.1 \times 10^{-4}$ and $< 2.5 \times 10^{-6}$ for Fd1 and Fd2, respectively. The kinetic models and the best-fit parameters corresponding to traces $a_{fit}$ (fitting data between 0 and 0.5 ms) and $b_{fit}$ (fitting data between 0 and 4 ms) are discussed in the text. In both cases, the final amplitudes of these fits were constrained to be equal to the red line signal. Note the break in timescale at 5 ms for trace b.

### *3.9. Kinetics of $Fd_{red}$ oxidation by ferredoxin-$NADP^+$-oxidoreductase (FNR)*

*In vitro* kinetic studies of $Fd_{red}$ oxidation by soluble partners have been reported in the case of FNR [24], NiR [54] and nitrate reductase [83]. A similar approach has been performed here. Flash-induced absorption kinetics are recorded using mixtures of PSI, Fd and the Fd-partner. In these conditions, the soluble partners FNR and NiR are reduced after $Fd_{red}$ dissociation from PSI and then diffusion to FNR or NiR. This corresponds to photosynthetic conditions, where the PSI-acceptor side reactions are initiated by PSI photoexcitation followed by Fd reduction, $Fd_{red}$ dissociation and partners reduction. In such experiments, however, only association rates can be studied for FNR and NiR reduction by $Fd_{red}$.

FNR reduction by $Fd1_{red}$ and $Fd2_{red}$ was measured by flash-absorption spectroscopy at 580 nm (Fig. 8). Under photosynthetic conditions, FNR catalyzes the 2-electron reduction of $NADP^+$ into NADPH by hydride transfer from its fully reduced form containing $FADH^-$ to $NADP^+$ [84]. The catalytic cycle involves sequential reduction of FAD by $Fd_{red}$, with Fd binding to FNR at a single site. The intermediate semiquinone redox state of FNR, $FNR_{sq}$, contains $FADH^{\bullet}$ which strongly absorbs at 580 nm, whereas $FADH^-$ does not. In the present experiments performed in the absence of the $NADP^+$ substrate, FNR is in large excess over PSI and hence over the $Fd_{red}$ produced after a single PSI turnover flash. It can then be hypothesized that $FNR_{sq}$ is primarily formed with only a minor involvement of $FNR_{red}$ (see however below the special case of Fd2) and $FADH^-$ since the binding of a second $Fd_{red}$ would be required following the dissociation of the firstly-bound Fd from $FNR_{sq}$.

Remarkably, a much slower $FNR_{sq}$ formation is observed with $Fd2_{red}$ than with $Fd1_{red}$ (Fig. 8). The signal at 1 ms, a time where mostly irreversible and single reduction of FNR is occurring (see further explanations below), is thus 100-times larger with Fd1 than with Fd2 (see numbers in Fig. 8 legend).

However, for a quantitative comparison of the second-order rate constants $k_{on}$ of FNR reduction by $Fd1_{red}$ or $Fd2_{red}$, one must take into account the fact that the full extent of $FNR_{sq}$ formation is observed neither with Fd1 nor with Fd2. Indeed, this full extent would give a signal corresponding to the red line in Fig. 8 (see Supp. Fig. 14 for the procedure to measure this signal level). The reasons for the incomplete formation of $FNR_{sq}$ are likely different for Fd1 and Fd2. In the case of Fd1, this is attributed to an incomplete forward reaction in the equilibrium $Fd1_{red} + FNR_{ox} \leftrightarrow Fd1_{ox} + FNR_{sq}$, due to the small value of the reaction constant ($K_{eq} = 1.26$, corresponding to ~72% of $FNR_{sq}$ formation in the conditions of Fig. 8; see Supp. Fig. 14 for the $K_{eq}$ determination). Such an incomplete reaction is consistent with the small difference in midpoint potentials between $Fd1_{red}$ ($E_m = -370$ mV) and previously reported values of $E_m(FNR_{ox}/FNR_{sq})$ at pH 8.0, *e.g.* −402 mV for spinach FNR [85] and −378 mV for *Syn.* 6803 FNR [24]. Indeed, with $K_{eq} = 1.26$, one can estimate the $E_m(FNR_{ox}/FNR_{sq})$ at −364 mV, very close to that of Fd1: $E_m(FNR_{ox}/FNR_{sq}) = E_m(Fd_{ox}/Fd_{red}) + (RT/F) \times Ln(K_{eq})$.

In the case of Fd2, which has a midpoint potential at ~ −440 mV, significantly lower than that of the $(FNR_{ox}/FNR_{sq})$ couple, $K_{eq}$ should not be a limiting factor for FNR reduction. In this case, we hypothesize that the first step of FNR reduction by $Fd_{red}$ is so slow that the probability of a second FNR reduction, *via* slow Fd-catalyzed dismutation of $FNR_{sq}$ [24] cannot be neglected. This means that during the full $Fd_{red}$ oxidation, some $FNR_{red}$ is formed together with $FNR_{sq}$, thus decreasing the final amount of $FNR_{sq}$ and consequently the 580 nm signal amplitude. The final amount of $FNR_{sq}$ formed at long times (> 100 ms) in the presence of Fd2 may also be decreased by slow processes such as $O_2$ reduction by $Fd_{red}$ and $FNR_{sq}$, or electron recombination between $P700^+$ and $Fd2_{red}$, *via* uphill population of $(FA\ FB)_{1red}$ from $Fd2_{red}$.

Therefore the $k_{on}$ values were determined by fitting only the initial formation of $FNR_{sq}$ with the constraint that the extrapolated fitted amplitudes should correspond to 100% of $FNR_{sq}$. The validity of this assumption relies on the fact that neither the reverse reaction (electron transfer from $FNR_{sq}$ to $Fd_{ox}$ in the case of Fd1) nor the second FNR reduction (in the case of Fd2), nor $Fd_{red}/FNR_{sq}$ oxidation by $O_2$, nor recombination between $P700^+$ and $Fd_{red}$, should be significant at the onset of $FNR_{sq}$ formation.

A monoexponential rate $k_{obs}$ of $3.6\ s^{-1}$ was thus obtained for Fd2 (trace $b_{fit}$). From this rate and under the present conditions of first-order approximation ($[FNR_{ox}] = 7.79\ \mu M \gg [Fd_{red}]$, $k_{obs} = k_{on} \times [FNR]$), we obtained a rate constant $k_{on}$ of $4.6 \times 10^5\ M^{-1}\ s^{-1}$ for Fd2 (Table 5).

For Fd1, the initial signal rise is sigmoidal, which indicates the presence of a limiting step preceding $FNR_{sq}$ formation. One can exclude $Fd_{red}$ dissociation from PSI, as its rate is larger than $1 \times 10^4\ s^{-1}$ [51], which is too large to contribute to the signal sigmoidicity. Therefore,

**Table 5**
Second-order rate constants of $FNR_S$ and NiR reduction by Fd1 and Fd2.
Absolute values are shown in bold characters whereas two types of ratios (Fd2/Fd1 for a given partner and NiR/$FNR_S$ for a given Fd) are also given.

| | Fd1 | Fd2 | Fd2/Fd1 ratio of rate constants |
|---|---|---|---|
| $FNR_S$ | $4.1 \times 10^8\ M^{-1}\ s^{-1}$ | $4.6 \times 10^5\ M^{-1}\ s^{-1}$ | 0.001 |
| NiR | $1.43 \times 10^8\ M^{-1}\ s^{-1}$ | $0.47 \times 10^8\ M^{-1}\ s^{-1}$ | 0.34 |
| FNR/NiR ratio of rate constants | 3.1 | 0.01 | |

the rate-limiting reaction should occur after $Fd_{red}$ association to $FNR_{ox}$, according to the reaction scheme: $Fd_{red} + FNR_{ox} \rightarrow Fd_{red}:FNR_{ox} \rightarrow Fd_{ox}:FNR_{sq}$. The rate limiting reaction could be first-order intracomplex ET itself or any step preceding it, as a conformational gating, or coupled to it, as FAD protonation. Using this scheme and fitting both trace a (trace $a_{fit}$) and other kinetics measured at different FNR concentrations between 0 and 0.5 ms (Supp. Fig. 14C), we determined the rates $k_{on} = 4.1 \times 10^8\,M^{-1}\,s^{-1}$ and $k_{limit} = 640\,s^{-1}$ for the two consecutive reactions. This $k_{on}$ value has the same order of magnitude as that previously measured with *Syn.* 6803 partners ($6.2 \times 10^8\,M^{-1}\,s^{-1}$, [24]).

Thus, the $k_{on}$ value of FNR reduction by $Fd_{red}$ is about three orders of magnitude smaller for Fd2 than for Fd1. As a control experiment, we also measured the kinetics of FNR reduction by Fd2 in the presence of 1 mM $NADP^+$. Kinetics were slightly faster than that without $NADP^+$ with a 20% increase in the initial signal rise. This is consistent with the small effect of $NADP^+$ addition previously observed with *Syn.* 6803 proteins [24].

### 3.10. Kinetics of $Fd_{red}$ oxidation by NiR

NiR reduces nitrite to ammonium in a six-electron reaction, where electrons are provided by $Fd_{red}$ one by one [86–88]. The NiR catalytic center is a siroheme, which becomes reduced after single reduction by $Fd_{red}$. The second cofactor of NiR, a [4Fe−4S] cluster, is most probably involved as an electron-transfer relay between the Fd and the siroheme. To compare the reactivity of Fd1 and Fd2 with NiR, we used the approach described above for FNR. The flash-absorption changes were measured at 520 nm, a wavelength where a large part of the absorption changes is attributed to $Fd_{red}$ oxidation with only a small contribution due to NiR (Fig. 9) [54]. The properties of the recombinant form of NiR from the green algae *Chlamydomonas reinhardtii* used here were found to be similar to those of spinach NiR [28], which itself has been studied by the same flash-absorption method with PSI and Fd from *Syn.* 6803 [54]. In this last study [50], the absorption changes were consistent with reduction of the siroheme of NiR, with only a minor contribution of the [4Fe−4S] cluster.

The kinetics of NiR reduction by Fd2 are slower than by Fd1, but the difference between the two Fds is much smaller than in the case of FNR (Fig. 9). With both Fds, increasing the NiR concentration 2- and 4-fold led to faster kinetics but unchanged final amplitudes, which shows that

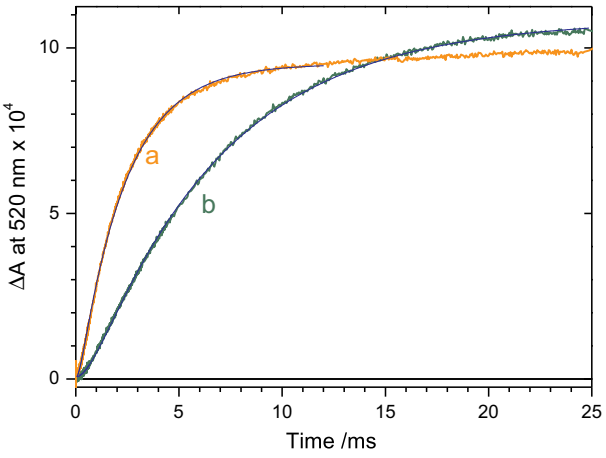


**Fig. 9.** Kinetics of NiR reduction by reduced Fd1 (trace a) and Fd2 (trace b) at pH 8.0.
The figure exhibits the kinetics of NiR reduction by $Fd_{red}$ as was the case in Fig. 8 for FNR. PSI and NiR concentrations were 0.243 μM and 3.11 μM, respectively. Similar concentrations of Fd were used in both cases (a: 4.73 μM Fd1; b: 4.71 μM Fd2). Both kinetics were fitted by an analytical function with 2 exponential components (see text): best-fit rates of ($441\,s^{-1}$, $5313\,s^{-1}$) and ($155\,s^{-1}$, $1398\,s^{-1}$) were obtained for traces a and b, respectively.

the reverse reaction from $NiR_{1red}$ to $Fd_{ox}$ can be neglected (Supp. Fig. 15).

The kinetics of NiR reduction by Fd1 and Fd2 exhibit a sigmoidal shape. In the case of Fd1, the sigmoidicity can be attributed to $Fd_{red}$ dissociation from PSI following light-induced reduction [51,89]. We will assume that it is also the case for Fd2. In the absence of reverse reaction, the following simplified kinetic model can be used: PSI:$Fd_{red}$ → free $Fd_{red}$ + $NiR_{ox}$ → $Fd_{ox}$ + $NiR_{1red}$ with rates $k_{off}$ and $k_2$ for the first and second reactions, respectively. Using the analytical expression derived from this scheme (see Supp. Fig. 15), the following best-fit values were determined: ($k_{off}$, $k_2$) = ($5313\,s^{-1}$, $441\,s^{-1}$) and ($1398\,s^{-1}$, $155\,s^{-1}$) for Fd1 and Fd2, respectively. Notably, $k_{off}$(Fd1) is smaller here than when studying FNR reduction ($k_{off} > 1 \times 10^4\,s^{-1}$), as reported in [3], because of the different salt concentrations and the presence of mannitol. From $k_2$, the second-order rate constants $k_{on}$ of NiR reduction ($= k_2/[NiR]$) were calculated to be $1.42 \times 10^8\,M^{-1}\,s^{-1}$ and $0.50 \times 10^8\,M^{-1}\,s^{-1}$ for Fd1 and Fd2, respectively. Moreover, by fitting kinetics at three different NiR concentrations with a global-fit procedure for each Fd, similar rate constants were obtained with $k_{on}$ values of $1.43 \times 10^8\,M^{-1}\,s^{-1}$ and $0.47 \times 10^8\,M^{-1}\,s^{-1}$ for Fd1 and Fd2, respectively (see Supp. Fig. 15). The Fd1 $k_{on}$ value is rather similar to that previously found for the spinach enzyme ($2.6 \times 10^8\,M^{-1}\,s^{-1}$, [54]) whereas the Fd2 $k_{on}$ is about 3-times smaller than that of Fd1. These $k_{on}$ values, as well as those measured with FNR, are summarized in Table 5. The table also displays ratios of $k_{on}$ values showing how a given partner discriminates between Fd1 and Fd2 (ratio Fd2/Fd1) and how a given Fd discriminates between FNR and NiR (ratio FNR/NiR).

### 3.11. Phylogeny of cyanobacterial Fds

A phylogenetic analysis of Fd2-like Fds in cyanobacteria was performed in 83 different cyanobacterial strains (for a total of 342 sequences), plus [2Fe-2S] Fds from a few eukaryotic Fds (the alga *C. reinhardtii*, the C3 plant *A. thaliana* and the C4 plant maize), for a total of 357 sequences. The phylogenetic tree is shown in Supp. Fig. 16A and a partial tree with only 26 different cyanobacterial strains is shown in Fig. 10 (see below how these 26 strains were chosen).

Interestingly, large branches can be defined by amino acids present at two positions, referred to as X and Y, and the branches were colored according to the identity of these amino acids. These positions were found to be important to distinguish Fd2 from Fd1. Position X corresponds to the residue following the second cysteine ligand (in the order of the amino-acid sequence) of the [2Fe−2S] cluster: Ser47 of the $Cys_{46}Ser_{47}Thr_{48}Cys_{49}$ motif in Fd1 and Val54 of the $Cys_{53}Val_{54}Asn_{55}Cys_{56}$ motif in Fd2. Position Y corresponds to the Phe residue that was found to be essential for FNR reduction by $Fd_{red}$ in previous studies: Phe65 and Phe72 in Fd1 and Fd2, respectively [18]. Sequence alignment shows that, for the vast majority of Fds, the positions X and Y are occupied by only two residues in each case and moreover the identity of the residues at the two positions is highly correlated (Table 6). Thus 47% and 46% of cyanobacterial Fds have X:Y = Ser:Phe (colored in red) or Thr:Gly (colored in green), respectively, corresponding to 160 and 156 sequences out of 342, respectively. Whereas Fd1 belongs to the first class (X:Y = Ser:Phe), Fd2, with X:Y = Val:Phe, is relatively atypical, as it does not belong to a major group. However, from the phylogenetic tree, Fd2 appears to belong to a well-defined sub branch of the red branch, which was colored in blue and contains 20 different Fds. In this blue branch, X:Y can take several values, the most frequent being Val:Phe, as in Fd2. Most of the other members of this group have Y = Phe (except 2 with Ile) whereas the identity of X is more variable (beside Val: Phe, Ile and Thr). It appears that in all cases, the side chain of X is bulkier than that of Ser.

The partial tree shown in Fig. 10 is made with all Fds from the 17 strains having a “blue” Fd plus those from 9 diverse strains, including *Nostoc* sp. PCC7120 and some being commonly studied. The tree structure is highly similar to that of the large tree and differs essentially

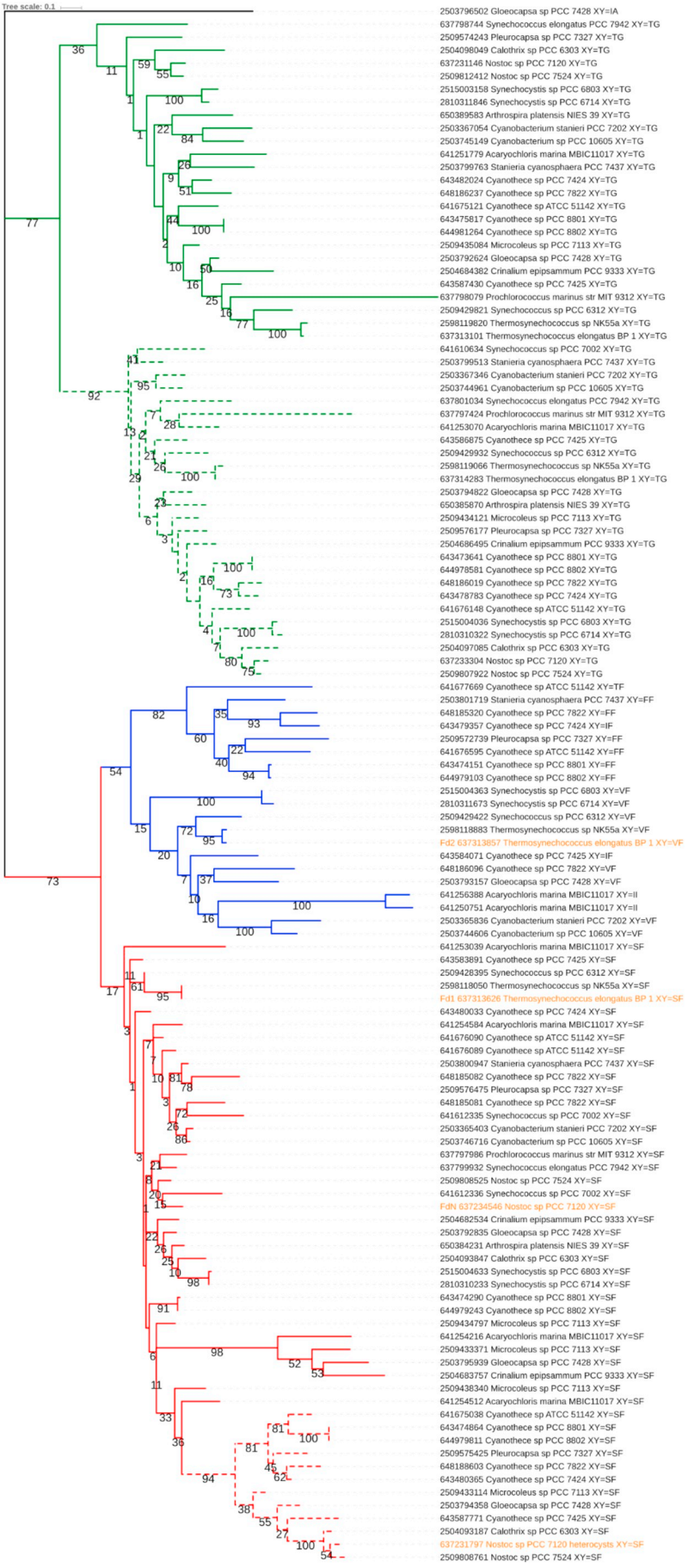


**Fig. 10.** Phylogenetic unrooted tree of all photosynthetic-type [2Fe−2S] Fds from 26 different cyanobacterial strains. The 17 strains having a Fd in the blue group (see text and Table 6) were considered, plus 9 other diverse strains. Sequence alignment was performed with MUSCLE and tree construction with the neighbor-joining method, both being provided in the SeaView software. Bootstrap values (from 0 to 100) were obtained from 1000 repetitions. The colors of the different branches (Table 6, Supp. Fig. 16) are defined according to the identity of the X:Y doublet: red for Ser:Phe; green and dashed light green for Thr:Gly, and blue for Val:Phe, Phe:Phe, Ile:Phe, Ile:Ile and Thr:Phe. Fd1, Fd2 and FdN are labelled in orange.

**Table 6**
Characteristics of the groups of cyanobacterial Fds from 83 different strains.

The colors (1st column) are those of the phylogenetic tree (Fig. 10 and Supp. Fig. 16A/B).

(a) All tested cyanobacteria have at least one (and up to 4) Fd from the red group, one Fd from the dashed light green group and most have one Fd from the green group.

(b) The major Fd isoforms presumably belong to this group. Moreover the major isoforms of *Arabidopsis thaliana* (Fd1/2/3; Fd3 = root isoform), maize (Fd1/2/3; Fd2 = bundlesheath isoform; Fd3 = root isoform) and *Chlamydomonas reinhardtii* (PetF) belong to this group (Supp. Fig. 16A).

(c) The number of Fds in each subgroup is indicated in subscript.

(d) 3 exceptions in the dashed light green group (X:Y = Ser:Gly in *Prochlorococcus marinus* NATL1A/NATL2A and *Prochlorococcus* sp. MIT0801) and 2 in the green continuous group (X:Y = Cys:Gly in *Prochlorococcus marinus* NATL1A/NATL2A).

| Fd group/color | Number of cyanobacterial Fds in each group[a] | Identity of the X:Y doublet of residues | Fds belonging to the group |
|---|---|---|---|
| Red | 160[b] | Ser:Phe | $Fd1_{T.\ elong.}$<br>$FdN_{Nostoc\ 7120}$<br>$Fed1_{Syn\ 6803}$<br>heterocyst $Fd_{Nostoc\ 7120}$ |
| Blue | 20 | $Val:Phe_9$[c]<br>$Phe:Phe_6$<br>$Ile:Phe_2$<br>$Ile:Ile_2$<br>$Thr:Phe_1$ | $Fd2_{T.\ elong.}$<br>$Fed4_{Syn\ 6803}$ |
| Green | 73 | Thr:Gly[d] | $Fed3_{Syn\ 6803}$, $Fd4_{T.\ elongatus}$ |
| Dashed light green | 83 | Thr:Gly[d] | $Fed2_{Syn\ 6803}$, $Fd3_{T.\ elongatus}$ |

only by the over-representation of "blue" Fds. Both trees suffer from relatively low bootstrap values, although those of the partial tree are better, especially regarding the base of the red branch. Low bootstrap values may be explained by the short size of Fd, which prevents to deduce any clear phylogenetic relationship. However, it is of note that the bootstrap value for the base of the blue branch is higher than for most red branches, which suggests a common evolutionary origin. The green branch is subdivided in two sub-branches, marked in green and dashed light green, this last one exhibiting a relatively high bootstrap value. This branch includes Fed2 from *Syn.* 6803, which was found to be involved in the response to changing environmental iron concentrations [13], as well as Fd3 from *T. elongatus*. All Fds from this branch contain a C-terminal extension (Supp. Fig. 16B for Fds from the partial tree).

With respect to the distribution of Fds, the following features are observable: all tested cyanobacteria possess at least one "red" Fd (X:Y = Ser:Phe), with one of these being presumably the main Fd isoform. They also possess one and only one Fd from the dashed light green group (X:Y = Thr:Gly, except in three cases where X:Y = Ser:Gly). Moreover, the vast majority of cyanobacteria possess one Fd from the continuous green group (Supp. Fig. 16B for strains from the partial tree and Table 6). Fed3 from *Syn.* 6803 and Fd4 from *T. elongatus* belong to this group. To our knowledge, no member of this last group has been functionally characterized yet.

The "blue" Fds were found in only a subset, *i.e.* subclades B and E, of the seven subclades labelled A to G that were identified in a recent phylogenetic study of cyanobacteria (Fig. 1 in [90], Supp. Fig. 16C). Notably, these subclades are relatively distant whereas E appears to have split off early during evolution of cyanobacteria [90]. We therefore hypothesize that Fd orthologs to the "blue" ones have been lost in most cyanobacteria during evolution. Deletion mutants of Fed4, the homolog of Fd2 in *Syn. 6803*, showed that Fed4 is not essential for the survival and growth of the cyanobacteria under laboratory conditions [5]. This suggests that these Fds have a role associated with a specific physiology or with environmental conditions, which remain to be identified.

## 4. Discussion

The structural and physicochemical properties of the minor-type Fd2 from *T. elongatus* present significant differences with the main and well-characterized Fd1-type Fds. In addition to a significantly different structure, Fd2 has a redox potential more negative than that of Fd1, which lies at the lower edge of those measured for photosynthetic Fds. Fd2 has also a slightly more rhombic Fe1 environment and different redox-sensitive vibrational signatures of the amide bonds and of the [2Fe−2S] cluster environment. All these differences with Fd1 result in different electron transfer properties with PSI, NiR, and strikingly with FNR, showing a strong discrimination against FNR. In the following, we discuss how the structural differences between Fd1 and Fd2 can explain their different redox, spectral, and ET transfer properties.

### 4.1. Structure-property relationships of the isolated protein Fd2 when compared to Fd1 and FdN

Fd1 and FdN have very high sequence homology, notably in the two domains comprising the cysteine ligands of the cluster (Table 1), very similar redox potentials, electronic properties and strikingly similar vibrational properties both in the oxidized and reduced states, as revealed by FTIR difference spectroscopy, which demonstrates similar protein reorganization and properties of the [2Fe−2S] cluster upon reduction. In contrast, the sequence of Fd2 shows differences with both Fd1 and FdN, which result in significantly different structural and functional properties.

In addition to specific N- and C-ter extensions, one main difference between Fd2 and Fd1 or FdN concerns the replacement of the sequence $Cys_{46}SerThrCys_{49}$ in Fd1 (with Fd1 numbering) by the sequence $Cys_{53}ValAsnCys_{56}$ in Fd2 (Fd2 numbering). A number of other key amino acids also affect the structure of Fd2, notably in the region of loop 2 and hydrogen-bonding networks involved in Fd function.

Although the redox potential of Fds probably depends significantly on short- and long-range effects, the $Cys_{46}SerThrCys_{49}$ motif has been related in the past to the redox properties of Fds [65,91,92]. In addition, it was shown in FdN that reduction of the [2Fe−2S] cluster is accompanied by a flip of the peptide bond between Cys46 and Ser47 directed toward the bridging sulfur S2 for $FdN_{ox}$ [14]. Therefore, the specific $Cys_{53}ValAsnCys_{56}$ sequence in Fd2 could affect the properties of the [2Fe−2S] cluster both in the oxidized and reduced forms of Fd and explain in part the $\approx -70$ mV lower midpoint potential of Fd2 compared to Fd1.

Structural and vibrational properties of Fd1 and Fd2 show that the [2Fe−2S] cluster itself has similar structures in the two Fds, while its interactions with the Cys ligands and the protein are significantly different in Fd1 and Fd2. Similar structures of the [2Fe−2S] cluster in Fd1 and Fd2 are inferred by the $\nu$(Fe−Sb) IR modes, which are very sensitive markers of the Fe−Sb bond properties [75,76]. The frequencies of

these modes are identical for FdN and Fd1, and only 1 to 3 $cm^{-1}$ lower for Fd2 both in the oxidized and reduced Fds. In contrast, different orientations and hydrogen bonding interactions of the Cys ligands with the [2Fe−2S] cluster are inferred by the lower frequencies (−4 to −7 $cm^{-1}$) of the $\nu$(FeIII−St) and $\nu$(FeII−St) IR modes in both $Fd2_{ox}$ and $Fd2_{red}$, as compared to Fd1 and FdN (Table 4) [74,75,77,80]. Different interactions of the Cys ligands of the [2Fe−2S] cluster with the protein are also clearly identified in the structure of Fd2, as detailed in the Results section (Section 3).

It is to note that the $Cys_{53}ValAsnCys_{56}$ motif of Fd2 has direct consequences on the different hydrogen bonding interactions formed by the Cys53 ligand of the [2Fe−2S] cluster (Table 3). In $Fd2_{ox}$, Cys53/S$\gamma$ forms two hydrogen bonds with peptide NH groups only, while in Fd1, the corresponding Cys46/S$\gamma$ is involved in an additional and specific hydrogen-bonding network, that involves both the Ser40 hydroxyl group and the side chain hydroxyl of Thr48 from the $Cys_{46}SerThrCys_{49}$ motif (Table 3, Suppl. Fig. 10B). Structural differences at the level of the Cys ligands probably contribute to the different midpoint potentials of Fd1 and Fd2. Notably, the specific interactions formed by Cys46/S$\gamma$ in Fd1 have led to the hypothesis that Cys46 could be protonated and at the origin of the redox-sensitive Cys $\nu$(SH) IR mode observed for Fd1 only. Analysis of site-directed mutants is needed to further explore this hypothesis, since involvement of the Cys87 in this IR band is an alternative possibility.

Some structural differences between Fd2 and the Fd1-type ferredoxins may not affect the redox potential of the Fd but its electron transfer properties. This concerns the surface charge distribution and dipole moment, but also hydrogen bonding interactions such as the interactions between residues Asp66 and Lys76 near loop 2 and the residues Arg4 and Ala108 of the N or C terminus, respectively, in Fd2, which have no equivalents in Fd1 (Fig. 4-A B). Importantly, the structure of Fd2 shows differences with Fd1 in the structure of loop 2, due notably to the presence of His70 in place of Gln63 in Fd1 and different orientation of Phe72 and hydrogen bonding networks that may explain the differences in electron transfer properties of Fd1 and Fd2 with their redox partners, in particular with FNR.

### 4.2. Diffusion-limited ET rates between Fd and its partners PSI, FNR and NiR

The present work provides evidence for large differences between Fd1 and Fd2 regarding the kinetics of ET reactions and the association rates with their ET partners PSI, FNR and NiR. Moreover, there is no precedence that time-resolved ET kinetics were determined for an alternative photosynthetic Fd. We found that Fd2 reacts less efficiently than Fd1 with the three studied partners PSI, FNR, and NiR, but the difference in reactivity was strikingly much larger with FNR. The second-order ET rate constant was three-orders of magnitude smaller for FNR reduction by Fd2 compared to Fd1, while it was about three times slower for NiR reduction or for reduction by PSI. These data demonstrate that Fd2 exerts a strong discrimination against FNR that may correspond to a physiological role different from that of Fd1.

With regard to past literature, reduction by PSI of an overexpressed minor Fd of *Arabidopsis*, FdC1, was reported [93]. This process was measured *via* cytochrome *c* reduction (by $Fd_{red}$) under continuous illumination and a 14-fold decrease in the Michaelis constant $K_m$ was found *vs* the main Fd. FdC1 has a relatively high midpoint potential (−281 mV, *ibid*) and may not be primarily expressed in leaves [94], which would be in line with its poor reactivity with PSI. In a different approach, site-directed mutants of FdN studied with a low time resolution [95] showed that the effects of mutations are much smaller when looking at reduction by PSI than when looking at reduction of FNR by $Fd_{red}$, concluding that Fd reduction by PSI is relatively robust toward amino-acid substitutions. This is in agreement with the different reactivity of Fd2 *vs* Fd1, which is much larger with FNR than with PSI.

The 3-fold decrease in Fd2 *vs* Fd1 in the second-order rate constant of ET with PSI and NiR is probably due to a less efficient Fd2 electrostatic steering [96–99] leading to complex formation, which can be attributed to the smaller Fd2 negative charge and/or to a less favorable orientation of its electric dipole moment, as these two parameters are dramatically different between Fd1 and Fd2 (Fig. 3, Supp. Table 2). On the other hand, it can be also reasonably assumed that the ET efficiency, *i.e.* the probability of electron transfer before complex dissociation, is high for both Fd2 and Fd1 with PSI and NiR.

In the case of the FNR reduction by Fd2, the very small second-order rate of this process may involve both an inefficient steering and a poor ET efficiency. Such a poor efficiency means that the dissociation rate of the $Fd2_{red}$:FNR complex would be faster than intracomplex ET. The question then arises whether one can identify Fd2 structural features that impede the formation of a stable and functional complex with FNR. It is also worth considering the details of the partners interface for interpreting the intracomplex first-order kinetics of Fd2 reduction by PSI. Both issues will be discussed in the following paragraphs.

### 4.3. Intracomplex reduction of Fds by PSI

The PSI:Fd intracomplex kinetics of Fd reduction by $(F_A\ F_B)_{1red}$ are significantly different with Fd1, Fd2 and Fd1'. This can be attributed to differences in either driving force or electronic coupling. Most remarkably, the Fd2 kinetics are especially slow, with the absence of a sub-μs component and a single relatively slow phase of 140 μs halftime. This is in contrast with previous studies where a sub-μs phase has always been observed together with one or two components with $t_{1/2}$ in the 3–100 μs time range [100].

The slow Fd2 kinetics may be due to a strong decrease in the ET electronic coupling for intracomplex Fd reduction with Fd2 *vs* Fd1, due *e.g.* to steric hindrance leading to a large increase in the distance between the Fd [2Fe−2S] cluster and the terminal PSI acceptor $F_B$. To test this possibility, we aligned the Fd2 structure to that of Fd1 in the structure of the PS:Fd1 complex. It was thus found that steric hindrance occurs for several pairs of residues of PSI and Fd2: Arg40 in PsaA and Asp69 in Fd2, Arg36 on PsaA and Asp79 in Fd2, and Lys34 on PsaA and Tyr46 in Fd2 (Supp. Fig. 17A). While a very strong steric clash is involved for the Arg40PsaA/Asp69Fd2 pair, only a limited steric hindrance is involved for the other pairs. These steric constraints may then lead to a significant rearrangement of the PSI:Fd2 structure, as compared to that of PSI:Fd1, which in turn would result in a strong decrease in the ET coupling. However an alternative possibility exists, that the initial sub-μs intracomplex Fd2 reduction is negligible due to a small equilibrium constant $K_{ET}$ of the reaction: $PSI_{red}:Fd_{ox} \rightarrow PSI_{ox}:Fd_{red}$, so that Fd2 reduction would proceed *via* energetic relaxation of the $PSI_{ox}:Fd2_{red}$ and/or fast dissociation of $Fd2_{red}$ from PSI. As this point is outside the main scope of the paper, it will not be discussed further (some details are given in Supp. Fig. 17B).

### 4.4. FNR reduction by Fd2

As mentioned above, the Fd2:FNR complex is either highly transitory (fast dissociation) or ET-reaction incompetent, or both. In all X-ray structures of photosynthetic supercomplexes involving Fd, *i.e.* with PSI (PDB ID: 2PVO [17]), FNR (PDB ID: 1EWY [16], 1GAQ [101] and 5H5J, [102]), sulfite reductase (PDB ID: 5H8Y and 5H92 [103]) and ferredoxin:thioredoxin reductase (PDB ID: 2PVO [104]), the [2Fe−2S] cluster of Fd is facing its interaction partner, so as to minimize the distance between the [2Fe−2S] cluster and the redox cofactor of its partner. Our data show that Fd2 cannot bind to FNR in such a favorable conformation, contrary to Fd1. This difference should result from differences in steric hindrance of complex formation, in surface charge distribution (Fig. 3 C and D) or in hydrogen bonding interactions at the Fd surface around its [2Fe-2S] cluster. For a better understanding, we made docking simulations using GRAMM-X (http://vakser.compbio.ku.edu/resources/gramm/grammx). This approach was able to reproduce

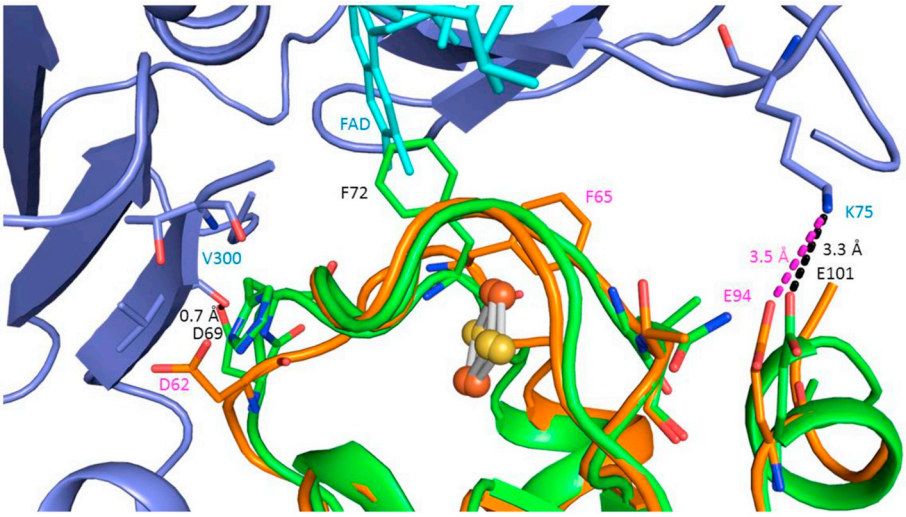


**Fig. 11.** Superposition of the interactions between the docking models obtained for Nostoc FNR (blue) and either Fd1 (orange) or Fd2 (green).
The FNR-Fd docking simulations were made using GRAMM-X (http://vakser.compbio.ku.edu/resources/gramm/grammx). It was possible to reproduce the structure obtained by crystallization for the FNR-Fd complex obtained with Nostoc FNR (from 1ewy, Dimer) and Nostoc Fd (from 1ewy [17]). A similar model could also be obtained using *Nostoc* FNR and *T. elongatus* Fd1 (from 5aui [22]). This was not possible using Nostoc FNR and *T. elongatus* Fd2. The differences between FNR from Nostoc and from *T. elongatus* cannot be the reason for the lack of interaction, since ClustalW Multiple sequence Alignment showed that the large differences between the *Nostoc* and the *T. elongatus* FNR sequences are the N-terminal length and some deletions, which are not close to the Fd binding site.
The environment around the coupling surface between FAD (light-blue)-binding Nostoc FNR (dark blue, PDB ID: 1ewy) and Fd1 (orange, PDB ID: 5aui) or Fd2 (green) is shown. The hydrogen bonds are shown with dashed lines in black and magenta for Fd2 and Fd1, respectively. The superimposition of the two complexes shows a comparable interaction between Glu101 in Fd2 or Glu94 in Fd1 and Lys75 in FNR. In contrast, the models show steric clash between the side chain of Phe72 in Fd2 and the FAD cofactor of FNR, and a too short distance between the side chain of Asp69 in Fd2 and Val300 peptide C═O of FNR.

the structure of the FNR:Fd complex obtained for *Nostoc*. We could also establish a docking model between the *Nostoc* FNR and *T. elongatus* Fd1 (Fig. 11), as expected from the fact that the FNRs of *Nostoc* and *T. elongatus* are highly similar in the Fd docking region. However, it was not possible to establish a complex between the *Nostoc* FNR and *T. elongatus* Fd2. Superposition of Fd2 with FdN in the FNR:FdN complex (PDBID: 1EWY, [16]) showed that there was a steric clash between Phe72 in Fd2 and FAD, the cofactor of FNR. In addition, Asp69 which belongs to loop 2 in Fd2 and Val300 in FNR were too close (0.7 Å, Fig. 11). From this model, we may identify the structural features of Fd2, which make it incompatible with the functional docking to FNR.

Among the large differences between the Fd1 and Fd2 structures, three are located at the Fd:FNR interface of the *Nostoc* complex: loop 2, the C-terminus (Tyr98 in Fd1, Leu105 to Ala108 in Fd2) and the $Cys_{46}SerThrCys_{49}$ motif, replaced by $Cys_{53}ValAsnCys_{56}$ in Fd2. Several features are involved in the differences in the loop 2 structure in Fd2. These are the bulkiness of His70 (corresponding to Gln63 in Fd1), the different hydrogen bonding patterns, involving Gly51-Phe72 in Fd2 and Gly44-Ser64 in Fd1 (Fig. 4A–B) and the orientation of the Phe72 in Fd2, which is totally different from that of Phe65 in Fd1 (Fig. 4C). Phe65 in Fd1 is close to the Cys46 and Ser47 residues belonging to the $Cys_{46}SerThrCys_{49}$ motif, whereas in Fd2, Phe72 is close to Ala52 in the same loop and this may be due to the bulkiness of Val54 in Fd2 as compared with Ser47 in Fd1.

In addition, an extended hydrogen bonding network exists in Fd1 between the side chain oxygen of Ser47 and one side chain oxygen of Glu94, and Ser47 further interacts with the terminal Tyr98 (Fig. 4B). The flipping of the peptide bond between Cys46 and Ser47 is considered as the redox structural switch responsible for the detachment of the Fd/PSI and Fd/FNR complexes [51,105]. In Fd2, Ser47 replacement by Val54 (and Tyr98 replacement by Leu105) could contribute to the differences in the electron transfer reactivity with FNR both by influencing the Phe72 orientation and the hydrogen-bonding network.

Previous studies showed that mutations of FdN at Phe65 (equivalent of Phe65 and Phe72 in Fd1 and Fd2) and at Glu94 decreased the rate of FNR reduction by three to four orders of magnitude [18]. While Phe65 and Glu94 are conserved between Fd1 and Fd2, the completely different orientation of Phe72 in Fd2 may contribute to the large decrease in FNR reduction kinetics. In contrast, the above substitutions in FdN were found to have negligible to moderate effects on electron transfer between FdN and PSI and NiR [86,95]. The same trend is observed when comparing Fd1 and Fd2, which suggests that differences between Fd1 and Fd2 in loop2 including Phe72/Phe65 orientation are of relatively little importance for Fd interactions with PSI and NiR.

### 4.5. Discrimination of Fd2 against FNR

Our data show that reduced Fd2 is almost unable to reduce FNR and thus cannot be involved in photosynthetic $NADP^+$ reduction, whereas it reduces NiR quite efficiently, even if 3-fold times less than Fd1. Many studies have been made in the past reporting some specificity of different Fds in ET-pathways or redox partners. Such evidence has been mostly obtained in plants, where different Fds are expressed in different parts of the plant (*e.g.* root *vs* leaf) or in different cell types of C4 plants (bundle sheat *vs* mesophyll in maize), either for favouring reverse electron flow (NADPH → FNR → Fd) or cyclic *vs* linear electron flow (reviewed in [106]). In the case of reverse electron flow occurring in roots, both specific Fd and FNR are involved, with a redox scaling ($E_m$(Fd) > $E_m$(FNR)) opposite to that in leaves [11,107]. In *Arabidopsis*, it was found that the minor ferredoxin FdC1 is unable to photoreduce $NADP^+$ *via* FNR, and this absence of activity was attributed to its high midpoint potential [93]. FdC1 can however interact with leaf-type electron acceptors including NiR, as with PSI, and can interact with FNR for reverse electron flow, albeit with a decreased efficiency [94]. The same authors showed that FdC1 might divert some reducing power away from FNR in *Arabidopsis* mutants overexpressing this Fd. Therefore, FdC1 looks rather similar to Fd2 in its functional properties, with a strong discrimination against FNR reduction. However, this discrimination was attributed to its midpoint potential being too high to reduce FNR, a feature that clearly differs from Fd2. In the case of *Equisetum*, two different Fds were found to behave similarly with regard to light-induced $NADP^+$ reduction using spinach membranes whereas only the reverse electron flow from NADPH to Fd was found to be somewhat different [108].

A minor Fd from *Chlamydomonas reinhardtii*, FdX2, was found to be more efficient in reducing NiR than the main Fd [12]. This Fd has a higher midpoint potential ($E_m$ = −321 mV) than the main Fd (−398 mV) and can interact efficiently with FNR for reverse electron flow, making it a root-like Fd. However, its ability to sustain $NADP^+$ photoreduction was not tested. In this context, it is worth noting that both FdC1 from *Arabidopsis* and FdX2 from *Chlamydomonas* lack the Phe residue which is indispensable for efficient FNR reduction in cyanobacteria and that this Phe was also shown, with cyanobacterial enzymes, not to be indispensable for reverse electron flow from NADPH to

Fd [109]. Impairment of the reverse electron flow from FNR to Fd has been rather associated to different charge distributions on the Fd in maize [110].

To our knowledge, the only case where functional comparison of different Fds have been yet performed in cyanobacteria concerns heterocyst-forming cyanobacteria. The heterocyst Fd has been found to be able to perform $NADP^+$ photoreduction with only a two-fold decrease in activity compared to the vegetative Fd [109] but it exhibits a positive discrimination for nitrogenase reduction [111]. It therefore appears that our study provides the first example of a strong discrimination against FNR of a minor Fd in cyanobacteria.

The phylogenetic analysis of most cyanobacterial Fds revealed that residues Ser/Val of the $Cys_{53}XXCys_{56}$ motif (Fd2 numbering) as well as the presence of Phe65/72 could discriminate large groups of Fds. In particular, all Fd1-like ferredoxins involved in photosynthetic electron transfer toward FNR presumably have a CysSerXCys motif and a Phe residue homologous to Phe65 in Fd1. In contrast, Fd2 belongs to a small class of 20 Fds (blue group in Fig. 10 and Supp. Fig. 16A) in which the Ser is substituted by a Val (9 sequences), a Phe (6 sequences) or an Ile (4 sequences) residue. From the phylogenetic analysis, we hypothesize that all Fds from this blue group exhibit discrimination against FNR, notably because of a different orientation of the Phe side chain in position Y, induced by the bulky residue in position X, while keeping a low midpoint potential. This group of ferredoxins is found only in cyanobacteria.

Another mode of discrimination against FNR may be present in all species with Fds belonging to the green group of Fig. 10, having a Thr in place of the Ser and a Gly in place of the Phe residue, previously found to be essential for FNR reduction from a mutational analysis of FdN [18]. Fed2 and Fed3 from *Syn. 6803*, corresponding to Fd3 and Fd4 in *T. elongatus*, are members of this "green group". The impossibility to generate deletion mutants concluded to their indispensable role in *Synechocystis* [5]. Fed2 has been recently shown to have a midpoint potential of −243 mV *vs* NHE, indicating that it cannot function in photosynthetic electron transport by reducing FNR or other Fd-dependent enzymes as NiR. In contrast, it has been shown to play a role in the response to low-level iron, possibly related to its specific C-terminal extension [13]. Unfortunately, no Fd from this group has been studied so far structurally, although one gene copy of such Fd is present in each cyanobacterial strain sequenced to date.

Fd2 is therefore the first example of a highly characterized minor Fd with strong homology with Fd1, keeping a low redox Em, while showing unique structural features and discrimination against FNR.

### 4.6. Contribution of Fd2 to photosynthetic electron flow

As Fd2 is about 20 times less abundant than Fd1 and exhibits both slower reduction kinetics and a lower affinity for PSI than Fd1, it can be asked whether it can be significantly photoreduced *in vivo*. In darkness, the excess of Fd1 over Fd2 combined with the > 3-fold lower affinity of Fd2 for PSI is expected to lead to a large excess of PSI binding Fd1 *vs* Fd2. In turn, it is expected that little $Fd2_{red}$ will be produced under conditions where most of Fd is oxidized, *i.e.* under very low light as well as just after a dark period. The situation should be quite different under continuous illumination. Firstly, the affinity of Fd1 for PSI is much decreased upon its reduction ($K_d$ > 10 μM, [51]), as expected for efficient turnover; secondly the Fd1 excess over PSI is probably small, if we assume that it is similar to that found in *Syn.* 6803, where a Fd/PSI ratio of *c.* 1/1 was measured [23]. Therefore part of PSI will rapidly release Fd1 as soon as it is reduced and/or bound to FNR and will be then available for binding Fd2 for its reduction.

$NADP^+$ photoreduction has been measured *in vivo* to be a fast process in *Syn.* 6803, with *e.g.* half of the final NADPH signal produced at 8 ms after a saturating light flash [112]. Very similar kinetics were observed for *T. elongatus* cells (P. Sétif, unpublished observations). This points to a very efficient process of FNR reduction by $Fd1_{red}$. Allocating reducing equivalents to other processes may then be of utmost importance for cell growth as this involves many different anabolic processes including nitrogen assimilation. Fd2 may play this role under conditions where little Fd1 would be available for partners other than FNR. In this context, a moderate decrease in Fd2 reactivity for its partners (as is the case with NiR) may be of minor importance as long as electron donation by $Fd2_{red}$ is not rate-limiting. Finally and importantly, the low midpoint potential of Fd2 *vs* that of Fd1 indicates that Fd2 should play its role mostly under photosynthetic conditions where it can be reduced by PSI.

## Transparency document

The Transparency document associated with this article can be found, in online version.

## Data deposition

The atomic coordinates and structure factors of the minor ferredoxin Fd2 coded by *tlr1236* and the major ferredoxin Fd1 coded by *tsl1009* from *Thermosynechococcus elongatus* have been deposited in the Protein Data Bank (www.rcsb.org) with the accession codes 6IRI and 6JO2, respectively.

## Acknowledgements

We thank the staff members at beamlines BL38XU, BL41XU and BL44XU of SPring-8 for their help in data collection. We also thank Dr. Shin-ichiro Yonekura for property analysis of Fd2. Dr. Corine Cassier-Chauvat, and Dr. Ghada Ajlani are acknowledged for useful discussions. We thank Gwenaëlle Moal for the genetic construction of the FNR expression vector and Dr. Bernard Lagoutte for FNR purification. PS thanks Dr. François André and Fernando Muzzopappa for discussing phylogeny issues and for help in the use of the dedicated softwares. This work was supported by a Program for Leading Graduate Schools program "Next generation picobiology pioneered by photon sciences" of MEXT, Japan. MS was supported by JSPS-KAKENHI grant in Scientific Research on Innovative Areas JP17H06435, a JSPS-KAKENHI grant 17K07367, and JRS was supported by a KAKENHI grant 17H06434. CB, RH, LZ and AB acknowledge support by the French Agence Nationale de la Recherche (ANR) under grant ANR-15PS2FIR. AB and PS were supported by the French Infrastructure for Integrated Structural Biology (FRISBI) ANR-10-INBS-05.

## Appendix A. Supplementary data

Supplementary data to this article can be found online at https://doi.org/10.1016/j.bbabio.2019.148084.

## References

[1] G. Hanke, P. Mulo, Plant type ferredoxins and ferredoxin-dependent metabolism, Plant Cell Environ. 36 (6) (2013) 1071–1084.
[2] M. Shin, D.I. Arnon, Enzymic mechanisms of pyridine nucleotide reduction in chloroplasts, J. Biol. Chem. 240 (3) (1965) 1405.
[3] Schuller JM, Birrell JA, Tanaka H, Konuma T, Wulflhorst H, Cox N, Schuller SK, Thiemann J, Lubitz W, Setif P *et al*: Structural adaptations of photosynthetic complex I enable ferredoxin-dependent electron transfer. *Science* 2019, **363**(6424):257 − +.
[4] B.B. Buchanan, The path to Thioredoxin and redox regulation in chloroplasts, Annu. Rev. Plant Biol. 67 (2016) 1–24.
[5] C. Cassier-Chauvat, F. Chauvat, Function and regulation of ferredoxins in the cyanobacterium, synechocystis PCC6803: recent advances, Life (Basel, Switzerland) 4 (2014) 666–680.
[6] K. Fukuyama, Structure and function of plant-type ferredoxins, Photosynth. Res. 81 (3) (2004) 289–301.
[7] D.L. Williamssmith, R. Cammack, Oxidation-reduction potentials of cytochromes P-450 and ferredoxin in bovine adrenal - their modification by substrates and inhibitors, Biochim. Biophys. Acta 499 (3) (1977) 432–442.
[8] K. Tagawa, D.I. Arnon, Ferredoxins as electron carriers in photosynthesis and in

biological production and consumption of hydrogen gas, Nature 195 (4841) (1962) 537.
[9] R. Cammack, K.K. Rao, C.P. Bargeron, K.G. Hutson, P.W. Andrew, L.J. Rogers, Midpoint redox potentials of plant and algal ferredoxins, Biochem. J. 168 (2) (1977) 205–209.
[10] Y. Nakamura, T. Kaneko, S. Sato, M. Ikeuchi, H. Katoh, S. Sasamoto, A. Watanabe, M. Iriguchi, K. Kawashima, T. Kimura, et al., Complete genome structure of the thermophilic cyanobacterium Thermosynechococcus elongatus BP-1, DNA Res. 9 (4) (2002) 123–130.
[11] G.T. Hanke, Y. Kimata-Ariga, I. Taniguchi, T. Hase, A post genomic characterization of arabidopsis ferredoxins, Plant Physiol. 134 (1) (2004) 255–264.
[12] A.M. Terauchi, S.F. Lu, M. Zaffagnini, S. Tappa, M. Hirasawa, J.N. Tripathy, D.B. Knaff, P.J. Farmer, S.D. Lemaire, T. Hase, et al., Pattern of expression and substrate specificity of chloroplast ferredoxins from Chlamydomonas reinhardtii, J. Biol. Chem. 284 (38) (2009) 25867–25878.
[13] M. Schorsch, M. Kramer, T. Goss, M. Eisenhut, N. Robinson, D. Osman, A. Wilde, S. Sadaf, H. Bruckler, L. Walder, et al., A unique ferredoxin acts as a player in the low-iron response of photosynthetic organisms, P Natl Acad Sci USA 115 (51) (2018) E12111–E12120.
[14] R. Morales, M.H. Chron, G. Hudry-Clergeon, Y. Petillot, S. Norager, M. Medina, M. Frey, Refined X-ray structures of the oxidized, at 1.3 angstrom, and reduced, at 1.17 angstrom, [2Fe-2S] ferredoxin from the cyanobacterium Anabaena PCC7119 show redox-linked conformational changes, Biochemistry 38 (48) (1999) 15764–15773.
[15] Rypniewski WR, Breiter DR, Benning MM, Wesenberg G, Oh BH, Markley JL, Rayment I, Holden HM: Crystallization and structure determination to 2.5-a resolution of the oxidized [Fe2-S2] ferredoxin isolated from Anabaena-7120. *Biochemistry* 1991, **30**(17):4126–4131.
[16] R. Morales, G. Kachalova, F. Vellieux, M.H. Charon, M. Frey, Crystallographic studies of the interaction between the ferredoxin-NADP(+) reductase and ferredoxin from the cyanobacterium Anabaena: looking for the elusive ferredoxin molecule, Acta Crystallogr D 56 (2000) 1408–1412.
[17] H. Kubota-Kawai, R. Mutoh, K. Shinmura, P. Setif, M.M. Nowaczyk, M. Rogner, T. Ikegami, H. Tanaka, G. Kurisu, X-ray structure of an asymmetrical trimeric ferredoxin-photosystem I complex, Nature Plants 4 (4) (2018) 218–224.
[18] J.K. Hurley, Z. Salamon, T.E. Meyer, J.C. Fitch, M.A. Cusanovich, J.L. Markley, H. Cheng, B. Xia, Y.K. Chae, M. Medina, et al., Amino-acid-residues in Anabaena ferredoxin crucial to interaction with ferredoxin Nadp+ reductase - site-directed mutagenesis and laser flash-photolysis, Biochemistry 32 (36) (1993) 9346–9354.
[19] B. Baumann, H. Sticht, M. Scharpf, M. Sutter, W. Haehnel, P. Rosch, Structure of Synechococcus elongatus [Fe2S2] ferredoxin in solution, Biochemistry 35 (39) (1996) 12831–12841.
[20] H. Hatanaka, R. Tanimura, S. Katoh, F. Inagaki, Solution structure of ferredoxin from the thermophilic cyanobacterium Synechococcus elongatus and its thermostability, J. Mol. Biol. 268 (5) (1997) 922–933.
[21] R. Mutoh, N. Muraki, K. Shinmura, H. Kubota-Kawai, Y.H. Lee, M.M. Nowaczyk, M. Rogner, T. Hase, T. Ikegami, G. Kurisu, X-ray structure and nuclear magnetic resonance analysis of the interaction sites of the Ga-substituted cyanobacterial ferredoxin, Biochemistry 54 (39) (2015) 6052–6061.
[22] M. Suga, T.L. Lai, M. Sugiura, J.R. Shen, A. Boussac, Crystal structure at 1.5 angstrom resolution of the PsbV2 cytochrome from the cyanobacterium Thermosynechococcus elongatus, FEBS Lett. 587 (19) (2013) 3267–3272.
[23] G. Moal, B. Lagoutte, Photo-induced electron transfer from photosystem I to NADP(+): characterization and tentative simulation of the in vivo environment, Bba-Bioenergetics 1817 (9) (2012) 1635–1645.
[24] N. Cassan, B. Lagoutte, P. Setif, Ferredoxin-NADP(+) reductase - kinetics of electron transfer, transient intermediates, and catalytic activities studied by flash-absorption spectroscopy with isolated photosystem I and ferredoxin, J. Biol. Chem. 280 (28) (2005) 25960–25972.
[25] J.C. Thomas, B. Ughy, B. Lagoutte, G. Ajlani, A second isoform of the ferredoxin : NADP oxidoreductase generated by an in-frame initiation of translation, P Natl Acad Sci USA 103 (48) (2006) 18368–18373.
[26] A. Omairi-Nasser, C.V. Galmozzi, A. Latifi, M.I. Muro-Pastor, G. Ajlani, NtcA is responsible for accumulation of the small isoform of ferredoxin:NADP oxidoreductase, Microbiol-Sgm 160 (2014) 789–794.
[27] A. Korn, G. Ajlani, B. Lagoutte, A. Gall, P. Setif, Ferredoxin:NADP(+) oxidoreductase association with Phycocyanin modulates its properties, J. Biol. Chem. 284 (46) (2009) 31789–31797.
[28] M. Hirasawa, J.N. Tripathy, F. Sommer, R. Somasundaram, J.S. Chung, M. Nestander, M. Kruthiventi, M. Zabet-Moghaddam, M.K. Johnson, S.S. Merchant, et al., Enzymatic properties of the ferredoxin-dependent nitrite reductase from Chlamydomonas reinhardtii. Evidence for hydroxylamine as a late intermediate in ammonia production, Photosynth. Res. 103 (2) (2010) 67–77.
[29] O.B. Zeldin, M. Gerstel, E.F. Garman, RADDOSE-3D: time- and space-resolved modelling of dose in macromolecular crystallography, J. Appl. Crystallogr. 46 (2013) 1225–1230.
[30] A.J. Mccoy, R.W. Grosse-Kunstleve, P.D. Adams, M.D. Winn, L.C. Storoni, R.J. Read, Phaser crystallographic software, J. Appl. Crystallogr. 40 (2007) 658–674.
[31] W. Kabsch, Xds, Acta Crystallogr D 66 (2010) 125–132.
[32] S. French, K. Wilson, Treatment of negative intensity observations, Acta Crystallogr A 34 (Jul) (1978) 517–525.
[33] A. Vagin, A. Teplyakov, MOLREP: an automated program for molecular replacement, J. Appl. Crystallogr. 30 (1997) 1022–1025.
[34] P. Emsley, B. Lohkamp, W.G. Scott, K. Cowtan, Features and development of Coot, Acta Crystallogr D 66 (2010) 486–501.
[35] A.A. Vagin, R.A. Steiner, A.A. Lebedev, L. Potterton, S. McNicholas, F. Long, G.N. Murshudov, REFMAC5 dictionary: organization of prior chemical knowledge and guidelines for its use, Acta Crystallogr D 60 (2004) 2184–2195.
[36] V.B. Chen, W.B. Arendall, J.J. Headd, D.A. Keedy, R.M. Immormino, G.J. Kapral, L.W. Murray, J.S. Richardson, D.C. Richardson, MolProbity: all-atom structure validation for macromolecular crystallography, Acta Crystallogr D 66 (2010) 12–21.
[37] W.G. Touw, C. Baakman, J. Black, T.A.H. te Beek, E. Krieger, R.P. Joosten, G. Vriend, A series of PDB-related databanks for everyday needs, Nucleic Acids Res. 43 (D1) (2015) D364–D368.
[38] W. Kabsch, C. Sander, Dictionary of protein secondary structure - pattern-recognition of hydrogen-bonded and geometrical features, Biopolymers 22 (12) (1983) 2577–2637.
[39] W. DeLano, The PyMOL Molecular Graphics System, In., 1.2 edn DeLano Scientific, Palo Alto, 2002.
[40] M.A. Larkin, G. Blackshields, N.P. Brown, R. Chenna, P.A. McGettigan, H. McWilliam, F. Valentin, I.M. Wallace, A. Wilm, R. Lopez, et al., Clustal W and clustal X version 2.0, Bioinformatics 23 (21) (2007) 2947–2948.
[41] M. Goujon, H. McWilliam, W.Z. Li, F. Valentin, S. Squizzato, J. Paern, R. Lopez, A new bioinformatics analysis tools framework at EMBL-EBI, Nucleic Acids Res. 38 (2010) W695–W699.
[42] P. Emsley, K. Cowtan, Coot: model-building tools for molecular graphics, Acta Crystallogr D 60 (2004) 2126–2132.
[43] E. Krissinel, K. Henrick, Secondary-structure matching (SSM), a new tool for fast protein structure alignment in three dimensions, Acta Crystallogr D 60 (2004) 2256–2268.
[44] N.A. Baker, D. Sept, S. Joseph, M.J. Holst, J.A. McCammon, Electrostatics of nanosystems: application to microtubules and the ribosome, P Natl Acad Sci USA 98 (18) (2001) 10037–10041.
[45] L. Holm, P. Rosenstrom, Dali server: conservation mapping in 3D, Nucleic Acids Res. 38 (2010) W545–W549.
[46] A. Tovchigrechko, I.A. Vakser, Development and testing of an automated approach to protein docking, Proteins 60 (2) (2005) 296–301.
[47] A. Tovchigrechko, I.A. Vakser, GRAMM-X public web server for protein-protein docking, Nucleic Acids Res. 34 (2006) W310–W314.
[48] W. Kabsch, Solution for best rotation to relate 2 sets of vectors, Acta Crystallogr A 32 (Sep1) (1976) 922–923.
[49] A. Boussac, K. Koyama, M. Sugiura, The Tll0287 protein is a hemoprotein associated with the PsbA2-photosystem II complex in Thermosynechococcus elongatus, Bba-Bioenergetics 1827 (10) (2013) 1174–1182.
[50] S.D. Bernardina, F. Alabarse, A. Kalinko, P. Roy, M. Chapuis, N. Vita, R. Hienerwadel, C. Berthomieu, P. Judeinstein, J.M. Zanotti, et al., New experimental set-ups for studying nanoconfined water on the AILES beamline at SOLEIL, Vib. Spectrosc. 75 (2014) 154–161.
[51] P. Setif, R. Mutoh, G. Kurisu, Dynamics and energetics of cyanobacterial photosystem I:ferredoxin complexes in different redox states, Bba-Bioenergetics 1858 (7) (2017) 483–496.
[52] P.Q.Y. Setif, H. Bottin, Laser flash absorption-spectroscopy study of ferredoxin reduction by photosystem-I in Synechocystis Sp Pcc-6803 - evidence for sub-microsecond and microsecond kinetics, Biochemistry 33 (28) (1994) 8495–8504.
[53] C.J. Batie, H. Kamin, Electron-transfer by ferredoxin-Nadp+ reductase - rapid-reaction evidence for participation of a ternary complex, J. Biol. Chem. 259 (19) (1984) 1976–1985.
[54] P. Setif, M. Hirasawa, N. Cassan, B. Lagoutte, J.N. Tripathy, D.B. Knaff, New insights into the catalytic cycle of plant nitrite reductase. Electron transfer kinetics and charge storage, Biochemistry 48 (12) (2009) 2828–2838.
[55] I. Chen, K. Chu, K. Palaniappan, M. Pillay, A. Ratner, J. Huang, M. Huntemann, N. Varghese, J.R. White, R. Seshadri, T. Smirnova, E. Kirton, S.P. Jungbluth, T. Woyke, E.A. Eloe-Fadrosh, N.N. Ivanova, N.C. Kyrpides, IMG/M v.5.0: an integrated data management and comparative analysis system for microbial genomes and microbiomes, Nucleic Acids Res. 47 (2019) D666–D667.
[56] U. Consortium, UniProt: a worldwide hub of protein knowkedge, Nucleic Acids Res. 47 (2019) D506–D515.
[57] M. Gouy, S. Guindon, O. Gascuel, SeaView version 4: a multiplatform graphical user interface for sequence alignment and phylogenetic tree building, Mol. Biol. Evol. 27 (2) (2010) 221–224.
[58] I. Letunic, P. Bork, Interactive tree of life (iTOL) v3: an online tool for the display and annotation of phylogenetic and other trees, Nucleic Acids Res. 44 (W1) (2016) W242–W245.
[59] Bottin H, Lagoutte B: Ferredoxin and Flavodoxin from the cyanobacterium Synechocystis Sp Pcc-6803. Biochim. Biophys. Acta 1992, 1101(1):48–56.
[60] A.V. Mishanina, M. Libiad, R. Banerjee, Biogenesis of reactive sulfur species for signaling by hydrogen sulfide oxidation pathways, Nat. Chem. Biol. 11 (7) (2015) 457–464.
[61] J.A. Simpson, S. Narita, S. Gieseg, S. Gebicki, J.M. Gebicki, R.T. Dean, Long-lived reactive species on free-radical-damaged proteins, Biochem. J. 282 (1992) 621–624.
[62] W.E. Blumberg, J. Peisach, Interpretation of electron-paramagnetic resonance-spectra of binuclear Iron-sulfur proteins, Arch. Biochem. Biophys. 162 (2) (1974) 502–512.
[63] P. Bertrand, J.P. Gayda, Theoretical interpretation of the variations of some physical parameters within the, 2fe-2s] Ferredoxin Group, Biochim. Biophys. Acta 579 (1) (1979) 107–121.
[64] H. Cheng, B. Xia, G.H. Reed, J.L. Markley, Optical, Epr, and H-1-Nmr spectroscopy of serine-ligated [2fe-2s] ferredoxins produced by site-directed mutagenesis of cysteine residues in recombinant Anabaena-7120 vegetative ferredoxins,

Biochemistry 33 (11) (1994) 3155–3164.
[65] J.K. Hurley, A.M. WeberMain, M.T. Stankovich, M.M. Benning, J.B. Thoden, J.L. Vanhooke, H.M. Holden, Y.K. Chae, B. Xia, H. Cheng, et al., Structure-function relationships in Anabaena ferredoxin: correlations between X-ray crystal structures, reduction potentials, and rate constants of electron transfer to ferredoxin:NADP(+) reductase for site-specific ferredoxin mutants, Biochemistry 36 (37) (1997) 11100–11117.
[66] S.Y. Venyaminov, N.N. Kalnin, Quantitative Ir spectrophotometry of peptide compounds in water (H2o) solutions .2. Amide absorption-bands of polypeptides and fibrous proteins in alpha-coil, Beta-coil, and random coil conformations, Biopolymers 30 (13–14) (1990) 1259–1271.
[67] M. Jackson, H.H. Mantsch, Protein secondary structure from Ft-Ir spectroscopy - correlation with dihedral angles from 3-dimensional Ramachandran plots, Can. J. Chem. 69 (11) (1991) 1639–1642.
[68] J. Kubelka, T.A. Keiderling, Differentiation of beta-sheet-forming structures: Ab initio-based simulations of IR absorption and vibrational CD for model peptide and protein beta-sheets, J. Am. Chem. Soc. 123 (48) (2001) 12048–12058.
[69] G. Zandomeneghi, M.R.H. Krebs, M.G. Mccammon, M. Fandrich, FTIR reveals structural differences between native beta-sheet proteins and amyloid fibrils, Protein Sci. 13 (12) (2004) 3314–3321.
[70] H. Susi, D.M. Byler, W.V. Gerasimowicz, Vibrational analysis of amino-acids - cysteine, serine, Beta-Chloroalanine, J. Mol. Struct. 102 (1–2) (1983) 63–79.
[71] V. Yatsyna, D.J. Bakker, R. Feifel, A.M. Rijs, V. Zhaunerchyk, Far-infrared amide IV-VI spectroscopy of isolated 2-and 4-Methylacetanilide, J. Chem. Phys. 145 (10) (2016).
[72] J. Bandekar, Amide modes and protein conformation, Biochim. Biophys. Acta 1120 (2) (1992) 123–143.
[73] Y. El Khoury, R. Hielscher, M. Voicescu, J. Gross, P. Hellwig, On the specificity of the amide VI band for the secondary structure of proteins, Vib. Spectrosc. 55 (2) (2011) 258–266.
[74] W.G. Fu, P.M. Drozdzewski, M.D. Davies, S.G. Sligar, M.K. Johnson, Resonance Raman and magnetic circular-dichroism studies of reduced, 2fe-2s, Proteins. Journal of Biological Chemistry 267 (22) (1992) 15502–15510.
[75] S. Han, R.S. Czernuszewicz, T. Kimura, M.W.W. Adams, T.G. Spiro, Fe2s2 protein resonance Raman-spectra revisited - structural variations among adrenodoxin, ferredoxin, and red paramagnetic protein, J. Am. Chem. Soc. 111 (10) (1989) 3505–3511.
[76] S. Han, R.S. Czernuszewicz, T.G. Spiro, Vibrational-spectra and normal mode analysis for [2fe-2s] protein analogs using S-34, Fe-54, and H-2 substitution - coupling of Fe-S stretching and S-C-C bending modes, J. Am. Chem. Soc. 111 (10) (1989) 3496–3504.
[77] Y. Mino, T.M. Loehr, K. Wada, H. Matsubara, J. Sandersloehr, Hydrogen-bonding of sulfur ligands in blue copper and iron sulfur proteins - detection by resonance Raman-spectroscopy, Biochemistry 26 (25) (1987) 8059–8065.
[78] M. Vidakovic, G. Fraczkiewicz, B.C. Dave, R.S. Czernuszewicz, J.P. Germanas, The environment of [2fe-2s] clusters in ferredoxins - the role of residue-45 probed by site-directed mutagenesis, Biochemistry 34 (42) (1995) 13906–13913.
[79] Y. El Khoury, P. Hellwig, A combined far-infrared spectroscopic and electrochemical approach for the study of Iron-sulfur proteins, Chemphyschem 12 (14) (2011) 2669–2674.
[80] V.K. Yachandra, J. Hare, I. Moura, T.G. Spiro, Resonance Raman-spectra of rubredoxin, desulforedoxin, and the synthetic analog Fe(S2-O-Xyl)2- - conformational effects, J. Am. Chem. Soc. 105 (21) (1983) 6455–6461.
[81] P.Q.Y. Setif, H. Bottin, Laser flash absorption-spectroscopy study of ferredoxin reduction by photosystem-I - spectral and kinetic evidence for the existence of several photosystem-I ferredoxin complexes, Biochemistry 34 (28) (1995) 9059–9070.
[82] C. Mignee, R. Mutoh, A. Krieger-Liszkay, G. Kurisu, P. Setif, Gallium ferredoxin as a tool to study the effects of ferredoxin binding to photosystem I without ferredoxin reduction, Photosynth. Res. 134 (3) (2017) 251–263.
[83] A.P. Srivastava, D.B. Knaff, P. Setif, Kinetic studies of a ferredoxin-dependent cyanobacterial nitrate reductase, Biochemistry 53 (31) (2014) 5092–5101.
[84] N. Carrillo, E.A. Ceccarelli, Open questions in ferredoxin-NADP(+) reductase catalytic mechanism, Eur. J. Biochem. 270 (9) (2003) 1900–1915.
[85] M.E. Corrado, A. Aliverti, G. Zanetti, S.G. Mayhew, Analysis of the oxidation-reduction potentials of recombinant ferredoxin-NADP(+) reductase from spinach chloroplasts, Eur. J. Biochem. 239 (3) (1996) 662–667.
[86] M. Hirasawa, J.N. Tripathy, R. Somasundaram, M.K. Johnson, M. Bhalla, J.P. Allen, D.B. Knaff, The interaction of spinach nitrite reductase with ferredoxin: a site-directed mutation study, Mol. Plant 2 (3) (2009) 407–415.
[87] S. Nakano, M. Takahashi, A. Sakamoto, H. Morikawa, K. Katayanagi, Structure-function relationship of assimilatory nitrite reductases from the leaf and root of tobacco based on high-resolution structures, Protein Sci. 21 (3) (2012) 383–395.
[88] U. Swamy, M.T. Wang, J.N. Tripathy, S.K. Kim, M. Hirasawa, D.B. Knaff, J.P. Allen, Structure of spinach nitrite reductase: implications for multi-electron reactions by the iron-sulfur : siroheme cofactor, Biochemistry 44 (49) (2005) 16054–16063.
[89] M. Hirasawa, G. Tollin, Z. Salamon, D.B. Knaff, Transient kinetic and oxidation-reduction studies of spinach ferredoxin-nitrite oxidoreductase, Bba-Bioenergetics 1185 (3) (1994) 336–345.
[90] P.M. Shih, D.Y. Wu, A. Latifi, S.D. Axen, Fewer DP, Talla E, Calteau A, Cai F, de Marsac NT, Rippka R *et al*: Improving the coverage of the cyanobacterial phylum using diversity-driven genome sequencing, P Natl Acad Sci USA 110 (3) (2013) 1053–1058.
[91] H. Uhlmann, R. Bernhardt, The role of threonine-54 in adrenodoxin for the properties of its iron-sulfur cluster and its electron-transfer function, J. Biol. Chem. 270 (50) (1995) 29959–29966.
[92] A.M. Weber-Main, J.K. Hurley, H. Cheng, B. Xia, Y.K. Chae, J.L. Markley, M. Martinez-Julvez, C. Gomez-Moreno, M.T. Stankovich, G. Tollin, An electrochemical, kinetic, and spectroscopic characterization of [2Fe-2S] vegetative and heterocyst ferredoxins from Anabaena 7120 with mutations in the cluster binding loop, Arch. Biochem. Biophys. 355 (2) (1998) 181–188.
[93] I. Voss, T. Goss, E. Murozuka, B. Altmann, K.J. McLean, S.E.J. Rigby, A.W. Munro, R. Scheibe, T. Hase, G.T. Hanke, FdC1, a novel ferredoxin protein capable of alternative electron partitioning, increases in conditions of acceptor limitation at photosystem I, J. Biol. Chem. 286 (1) (2011) 50–59.
[94] X.Q. Guan, S. Chen, C.P. Voon, K.B. Wong, M. Tikkanen, B.L. Lim, FdC1 and leaf-type ferredoxins channel electrons from photosystem I to different downstream electron acceptors, Front. Plant Sci. 9 (2018).
[95] J.A. Navarro, M. Hervas, C.G. Genzor, G. Cheddar, M.F. Fillat, M.A. Delarosa, C. Gomezmoreno, H. Cheng, B. Xia, Y.K. Chae, et al., Site-specific mutagenesis demonstrates that the structural requirements for efficient electron-transfer in Anabaena ferredoxin and flavodoxin are highly dependent on the reaction partner - kinetic-studies with photosystem-I, ferredoxin-Nadp(+) reductase, and cytochrome-C, Arch. Biochem. Biophys. 321 (1) (1995) 229–238.
[96] C.J. Camacho, Z.P. Weng, S. Vajda, C. DeLisi, Free energy landscapes of encounter complexes in protein-protein association, Biophys. J. 76 (3) (1999) 1166–1178.
[97] G. Castro, C.A. Boswell, S.H. Northrup, Dynamics of protein-protein docking: cytochrome c and cytochrome c peroxidase revisited, J. Biomol. Struct. Dyn. 16 (2) (1998) 413–424.
[98] R.R. Gabdoulline, R.C. Wade, Protein-protein association: investigation of factors influencing association rates by Brownian dynamics simulations, J. Mol. Biol. 306 (5) (2001) 1139–1155.
[99] N. Sinha, S.J. Smith-Gill, Electrostatics in protein binding and function, Curr Protein Pept Sc 3 (6) (2002) 601–614.
[100] P. Setif, Ferredoxin and flavodoxin reduction by photosystem I, Bba-Bioenergetics 1507 (1–3) (2001) 161–179.
[101] G. Kurisu, M. Kusunoki, E. Katoh, T. Yamazaki, K. Teshima, Y. Onda, Y. Kimata-Ariga, T. Hase, Structure of the electron transfer complex between ferredoxin and ferredoxin-NADP(+) reductase, Nat. Struct. Biol. 8 (2) (2001) 117–121.
[102] F. Shinohara, G. Kurisu, G. Hanke, C. Bowsher, T. Hase, Y. Kimata-Ariga, Structural basis for the isotype-specific interactions of ferredoxin and ferredoxin: NADP(+) oxidoreductase: an evolutionary switch between photosynthetic and heterotrophic assimilation, Photosynth. Res. 134 (3) (2017) 281–289.
[103] J.Y. Kim, M. Nakayama, H. Toyota, G. Kurisu, T. Hase, Structural and mutational studies of an electron transfer complex of maize sulfite reductase and ferredoxin, J Biochem-Tokyo 160 (2) (2016) 101–109.
[104] S.D. Dai, R. Friemann, D.A. Glauser, F. Bourquin, W. Manieri, P. Schurmann, H. Eklund, Structural snapshots along the reaction pathway of ferredoxin-thioredoxin reductase, Nature 448 (7149) (2007) 92–102.
[105] R. Morales, M. Frey, J.M. Mouesca, An approach based on quantum chemistry calculations and structural analysis of a [2Fe-2S*] ferredoxin that reveal a redox-linked switch in the electron-transfer process to the Fd-NADP(+) reductase, J. Am. Chem. Soc. 124 (23) (2002) 6714–6722.
[106] T. Goss, G. Hanke, The end of the line: can ferredoxin and ferredoxin NADP(H) oxidoreductase determine the fate of photosynthetic electrons? Curr Protein Pept Sc 15 (4) (2014) 385–393.
[107] Y. Onda, T. Matsumura, Y. Kimata-Ariga, H. Sakakibara, T. Sugiyama, T. Hase, Differential interaction of maize root ferredoxin : NADP(+) oxidoreductase with photosynthetic and non-photosynthetic ferredoxin isoproteins, Plant Physiol. 123 (3) (2000) 1037–1045.
[108] G. Kurisu, D. Nishiyama, M. Kusunoki, S. Fujikawa, M. Katoh, G.T. Hanke, T. Hase, K. Teshima, A structural basis of Equisetum arvense ferredoxin isoform II producing an alternative electron transfer with ferredoxin-NADP(+) reductase, J. Biol. Chem. 280 (3) (2005) 2275–2281.
[109] S. Schmitz, H. Bohme, Amino-acid-residues involved in functional interaction of vegetative cell ferredoxin from the cyanobacterium Anabaena Sp Pcc-7120 with ferredoxin-Nadp reductase, nitrite reductase and nitrate reductase, Bba-Bioenergetics 1231 (3) (1995) 335–341.
[110] T. Matsumura, Y. Kimata-Ariga, H. Sakakibara, T. Sugiyama, H. Murata, T. Takao, Y. Shimonishi, T. Hase, Complementary DNA cloning and characterization of ferredoxin localized in bundle-sheath cells of maize leaves, Plant Physiol. 119 (2) (1999) 481–488.
[111] Schmitz S, Schrautemeier B, Bohme H: Evidence from directed mutagenesis that positively charged amino-acids are necessary for interaction of nitrogenase with the [2fe-2s] heterocyst ferredoxin (Fdxh) from the cyanobacterium Anabaena Sp, Pcc7120. *Molecular and General Genetics* 1993, 240(3):455–460.
[112] J. Kauny, P. Setif, NADPH fluorescence in the cyanobacterium Synechocystis sp PCC 6803: a versatile probe for in vivo measurements of rates, yields and pools, Bba-Bioenergetics 1837 (6) (2014) 792–801.